Electrical and Gas-Sensing Properties of Micro-Nano Hierarchically Controlled Tin Dioxide Gas Sensors

MASHIBA, FELIPE H
九州大学大学院総合理工学府総合理工学専攻材料理工学メジャー

Master's Thesis

Electrical and Gas-Sensing Properties of Micro-Nano Hierarchically Controlled Tin Dioxide Gas Sensors

Science and Engineering of Materials and Devices

Interdisciplinary Graduate School of Engineering Sciences

Kyushu University

Student name Mashiba EelipeHiroshi

Supervisor

Data 2024/07/19

Contents

***Chapter 1*. Introduction**

1.1 Introduction 2
1.2 Metal oxide semiconductor gas sensors 3
1.2.1 Type of metal oxide semiconductor gas sensors 4
1.2.2 Reason for choosing SnO_2 5
1.2.3 Gas-sensing mechanism 7
1.2.4 Adsorption properties on SnO_2 9
1.3 Key factors design of metal oxide semiconductor gas sensors 14
1.3.1 Receptor function 14
1.3.2 Transducer function 17
1.3.3 Utility factor 20
1.4 MEMS gas sensors 23
1.4.1 A highly sophisticated approach – Pulse-driven temperature modulation 23
1.5 Motivation 25

***Chapter 2*. Experiments**

2.1 Introduction 27
2.2 Samples synthesis 27
2.2.1 Synthesis of SnO_2 nanoparticles 27
2.2.2 Classification of SnO_2 29
2.2.3 Synthesis of Pd-SnO_2 nanoparticles 30
2.3 Material evaluation 31
2.3.1 Crystal structure 31
2.3.2 Morphology observation 31
2.3.3 Pore properties and specific surface area 31
2.3.4 Particle size distribution 32
2.3.5 Catalytical evaluation 32
2.4 Manufacturing of sensor element 34
2.5 Sensor measurement methods 35
2.5.1 Resistance measurement system 36
2.5.2 Evaluation of sensor performance 37

***Chapter 3*. Classification of SnO_2 secondary particle**

3.1 Introduction 39
3.2 Classification of hydrothermally synthesized SnO_2 and their limitation 39
3.3 Characterization of classified SnO_2 – as-synthesized SnO_2 44
3.4 Characterization of top-down technique to fine-SnO_2 49
3.5 Summary 53

***Chapter 4*. Electrical and gas-sensing properties of secondary particle size-varied tin dioxide**

4.1 Introduction 55
4.2 Electrical and gas-sensing properties of hydrothermally synthesized SnO_2 on thick-film gas sensors with different secondary particle size 56
4.3 Electrical and gas-sensing properties of as-synthesized SnO_2 on miniaturized gas sensors with different secondary particle size 60
4.4 Electrical and gas-sensing properties of as-synthesized Pd-SnO_2 on miniaturized gas sensors with different secondary particle sizes 66
4.5 CO-catalytical combustion and TPR measurements 68
4.6 Summary 75
5.1 Conclusion 77
Reference 79
Acknowledgments 83

1. Introduction

1.1 Introduction
1.2 Metal oxide semiconductor gas sensors
1.2.1 Type of metal oxide semiconductor gas sensors
1.2.2 Advantages of SnO_2
1.2.3 Gas-sensing mechanism
1.2.4 Adsorption properties on SnO_2
1.3 Key factors design of metal oxide semiconductor gas sensors
1.3.1 Receptor function
1.3.2 Transducer function
1.3.3 Utility factor
1.4 MEMS gas sensor
1.4.1 A highly sophisticated approach – Pulse-driven temperature modulation
1.5 Motivation

1.1 Introduction

In the 20th century, new forms of energy were developed, including liquefied petroleum gas (LPG), a high-pressure gas. This new energy was incorporated into houses soon after, particularly in Japan. However, many LPG leakage accidents occurred, such as fire, explosion, poisoning, and asphyxiation [1-2]. Concomitantly, industries and automobiles emit exhaust gases that impact the environment, leading to the major problem of atmospheric greenhouse gases and affecting human health through the inhalation of specific gases [3]. To ensure safety and minimize environmental impact, it was crucial to monitor atmospheric gases before determining the next steps. Among a variety of gas sensors, semiconductor gas sensors were commercialized for domestic use, because of low cost and thermal stability. In 1952, Brattain and Bardeen of the Bell Laboratories, also known as inventors of the first working transistor, were the first to report that germanium modifies the electrical resistance depending on the atmosphere [4]. In 1953, Morrison reported that electrical conductivity changes that occurred in semiconductors as a function of ambient are related to the changes in the space charge layer at the surface [5]. Following that, in 1962, Seiyama et al. reported using a zinc oxide film that the electrical conductivity was modified with the adsorption or desorption of gas on the surface of the oxide [6]. At the same time, Taguchi, founder of Figaro Engineering Inc., patented the first semiconductor gas sensor using tin-oxide [7], starting to commercialize in 1968. After the obligatory incorporation of gas sensors in domestic ambient and the establishment of gas safety examination agencies [1], since the 1980s the number of gas leakage accidents has decreased [2]. Nowadays, the requisition of gas sensors is stricter, in which gas detection is limited to concentration in ppm (10^{-4} vol%) or ppb (10^{-7} vol%), mainly for environment VOC gas detection [8]. The advantages of metal oxide semiconductor gas sensors against other types are high thermal and chemical stability and high sensitivity to low gas concentration, with the potential to detect ppt (10^{-10} vol%) in severe conditions [9]. Such conditions include nanotechnology, catalyst application, heterostructure, conducting polymers, and miniaturization [10]. Correctly detecting the ppt level of gas concentration is crucial to the highly sophisticated use of gas sensors, such as medical diagnosis and health fitness [11].

Detection of diseases and physical conditions, such as cancer, diabetes,

Parkinson's and Alzheimer's disease, tuberculosis, asthma, and metabolism monitoring, is possible to realize by detection of some VOC gas [12] in ppt level. For that, the sensor device is required to avoid cross-detection, even for the same functional groups. The technology's implementation was crucial for the trillion-sensor project, serving as a network of intelligent gas sensors on the Internet of Things (IoT) [13]. The application is summarized in Table 1.1.

This chapter will introduce the characteristic and gas-sensing mechanism of metal oxide semiconductor gas sensors regarding the key design factor for highly sensitive and highly selective semiconductor gas sensors. With a focus on SnO_2, we will examine its adsorption and desorption properties, as well as its reaction properties, which are related to gas sensing. In this research, the effective material design appropriate for miniaturized gas sensors will be proposed, taking a major step toward the highly sophisticated use of miniaturized metal oxide semiconductor gas sensors.

Table 1.1 Application of gas sensors in various scenarios on the Internet of Things [13]

Environmental protection	Industrial / Agricultural	Public Safety	Medical Systems	Health Fitness	Home Auto.	Transportation
Air pollution	Flue	Toxins	Bedside	Wearable	Toxic gases	Exhaust
Waste	Emission	Explosives	Diagnostics	Biomarkers	Food safety	Traffic congestion
Water pollution					Allergens	

1.2 Metal oxide semiconductor gas sensors

Metal oxide semiconductor gas sensors can detect low gas concentration and high selectivity thanks to the nano-size effect of nanomaterial. Nanomaterials have a peculiar impact on optical, electrical, and chemical properties. The electron or hole mobility was drastically varied depending on particle size or geometry [14]. This subchapter will present the type of metal oxide semiconductor gas sensors, following the reason for choosing SnO_2 as a gas-sensitive material—furthermore, the metal oxide semiconductor gas-sensing mechanism and adsorption/desorption properties of related gases.

1.2.1 Type of metal oxide semiconductor gas sensors

The metal oxide semiconductor gas sensors can be categorized on their detective format: if it is electrical resistance format or not. Moreover, the electrical resistance format is separated into 2 types: surface reaction and bulk response [15] (Table 1.2). The surface reaction type gas sensor is the most used in all semiconductor gas sensors, in which the adsorbed or reacted gas on the surface modifies the electrical resistance of sensitive material. The relatively hardly reducible material such as SnO_2, ZnO, In_2O_3, and WO_3 operating under 500ºC is considered as surface control type. A detailed explanation of the sensing mechanism of this type is explored in subchapter 1.2.3. On the other hand, the bulk response type gas sensor is detected by the lattice defect modification. For example, the easily reducible material γ-Fe_2O_3, when in a reducible environment, reduces to form the low-resistance component in the bulk, maintaining the crystal structure: Fe_3O_4. Another example yet more modern is CeO_2. The CeO_2 intrinsically has exceptional redox properties, oxygen vacancies, and capacity that the charge easily modifies between Ce^{3+} and Ce^{4+} [16]. The high diffusion rates of oxygen vacancies generated by surface reactions affect the bulk electron properties due to their higher mobility, thus it is required to operate at higher temperatures than 500ºC [17]. The main figure of merit of the resistive type of gas sensor is sensor response S (=R_a/R_g) when R_a is electrical resistance in a carrier gas such as air and R_g is electrical resistance in target gas. This study will explore the SnO_2, a surface reaction resistive gas sensor.

Table 1.2 Electrical resistive-like semiconductor gas sensors [15]

Sensor element		Examples	Usage
Surface reaction	High porosity sint., thin, thick film	SnO_2+Pd, ZnO+Pd, $Ag_{0.04}V_2O_5$	Flammable gas, CO, NO_2, freon
Bulk response	High porosity sint.	γ-Fe_2O_3, $La_{1-x}Sr_xCoO_3$	LPG, Ethanol
	Sintered	TiO_2, CoO-MgO	Combustion obs.

1.2.2 Advantages of SnO_2

As mentioned in subchapter 1.2.1, SnO_2, ZnO, In_2O_3, and WO_3 are often used in gas sensors as sensitive materials. These materials were elaborated by their surface electrochemical properties. Since the electrical resistive-like semiconductor gas sensors (Table 1.2) depend on the surface reaction, the surface acidity [18], the activity of oxygen adsorbed on metal oxides [19,23], and the catalytic properties [20] are the most important factors in deciding which metal oxide is appropriate for high-performance gas sensors manufacturing.

The reactivity of the gas on a metal oxide surface is related directly to acid-base properties and catalytic properties. According to Tanaka et.al. [18], the electro-negativity of metal oxide is correlated to the p*K*a value (Fig. 1.1). The carbonates were formed on a metal oxide surface for a p*K*a value larger than 5, inhibiting the adsorption or reaction of analytes [21]. Especially, this is the main reason that SnO_2 is used instead of ZnO ($ZnCO_3$ or another carbonate group is formed in CO_2 exhibition). Except for this property, ZnO and SnO_2 are more appropriate and more popular metal oxides, which have been studied a lot in sensor literature since the invention of the gas sensor by Seiyama (ZnO) and Taguchi (SnO_2) [6,7].

The metal oxide semiconductors modify the surface carrier density with the presence of gas. The carrier density concentration near the surface depends on the adsorbates' number and type. Between them, oxygen is the main adsorbate. Table 1.3 shows the number of oxygen adsorbate temperatures below 560ºC [19]. Group A shows the absence of adsorbed oxygen. In other words, the surface lattice oxygen is active for any reaction. Group B (commonly p-type) exhibits many adsorbed oxygens, leading to active surface reactions, not necessarily modifying the electronic properties.

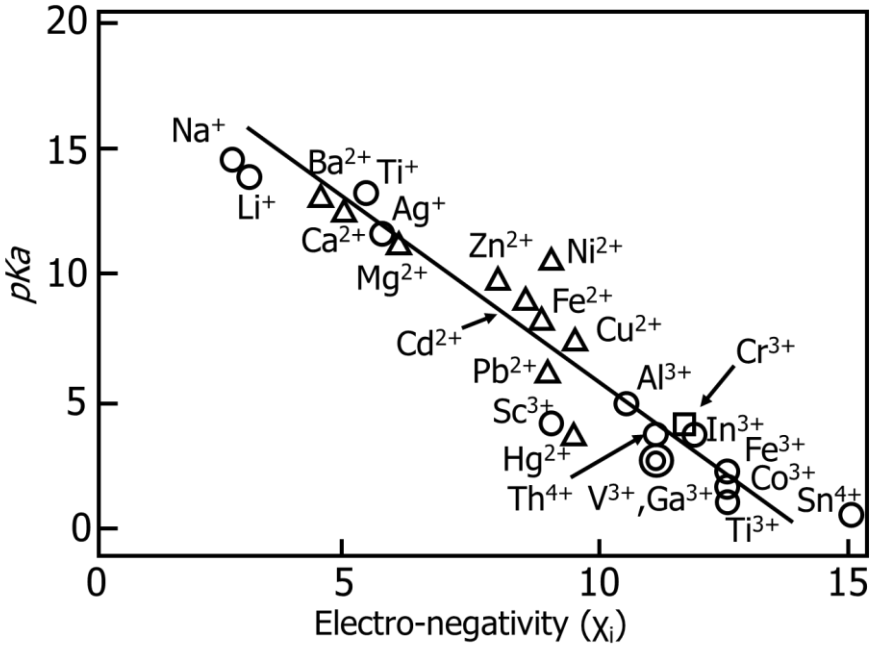

Fig. 1.1 Acid ionization constants for aqueous metal ions at 25ºC [18]

Table 1.3 Total oxygen amount desorbed until 560ºC for severe metal oxides [19]

Group	Oxides	Total oxygen amount desorbed until 560ºC
A	V_2O_5 (n)	0
	MoO_3 (n)	0
	Bi_2O_3 (p)	0
	WO_3 (n)	0
B	Cr_2O_3 (p)	2.13×10^{-2}
	MnO_2 (p)	6.54×10^{-2}
	Co_3O_4 (p)	3.30×10^{-2}
	NiO (p)	1.12×10^{-2}
	CuO (p)	1.42×10^{-2}
C	Fe_2O_3 (n)	4.05×10^{-3}
	TiO_2 (n)	5.52×10^{-5}
	ZnO (n)	2.45×10^{-4}
	SnO_2 (n)	2.11×10^{-3}

Group C exhibits a slight amount of oxygen, leading to moderate surface reactions that effectively alter the carrier concentration of the near-surface region. The latter group is more appropriate for gas sensors, at least in temperatures between 150ºC and 500ºC.

Recently, researchers have been investigating the effect of adsorbates of metal oxide on surface carrier density rather than adsorbed oxygen [22]. Since the main target gas of semiconductor gas sensors is generally focused on volatile organic compounds (VOC) gas, the support-sensitive material needs to have peculiar catalytic properties. For example, NiO and CuO are catalysts of propylene that promote complete combustion reactions. Alternatively, SnO_2 and ZnO promote the partial combustion reaction that produces benzene through aromatization followed by dimerization of dehydrogenated byproduct. Moreover, MoO_3 and Sb_2O_4 also promote the partial combustion reaction but produce acrolein through the addition of oxygen followed by a dehydrogenated byproduct [20]. These catalytic properties of metal oxide are one of the factors to determine the sensor performance: selectivity. A detailed explanation of sensor performance will be presented in Chapter 1.3.

The metal oxide for gas sensors must be thermally and chemically stable, have a moderate oxygen-adsorbed amount, and be catalytically active. For this reason, SnO_2 is more appropriate. SnO_2 is a tetragonal rutile crystal structure with a $P4_2/mnm$ space group, composed of SnO_6 octahedra [24]. A summary of the physical properties of SnO_2 is in Ref. (25). The SnO_2 shows high electrical conductivity even if the band gap is wide (3.6 V) [25]. This is because the formation energy of oxygen vacancies in the tin dioxide is low [26]. Such unique physical properties have made tin dioxide a widely used material for gas sensors.

1.2.3 Gas-sensing mechanism

As previously mentioned, n-type metal oxide semiconductor gas sensors detect gases through changes in electrical conductivity, provided by the reaction and desorption of adsorbates. The adsorbates such as oxygen have high electron affinity that can modify the surface physical properties of the semiconductor, such as work function, band bending, and electron affinity [27,28]. The type of adsorption that primarily changes the band bending is usually associated with ionized molecules. The ionized molecules trap electrons on the surface, creating the electron depletion layer, which eventually induces upward bending,

as shown in Fig. 1.2. The electrical resistance with this electronic configuration shows a high electrical resistance value. The adsorbates that do not have high electron affinity, form a surface dipole instead of electron trapping. The fact does not alter the bending of the band but decreases the localized electron affinity. Therefore, even though some adsorbates do not influence the electrical resistance of metal oxide semiconductors, indirectly modify the electronic configuration of the surface, altering the affinity to other active adsorbates [27,28].

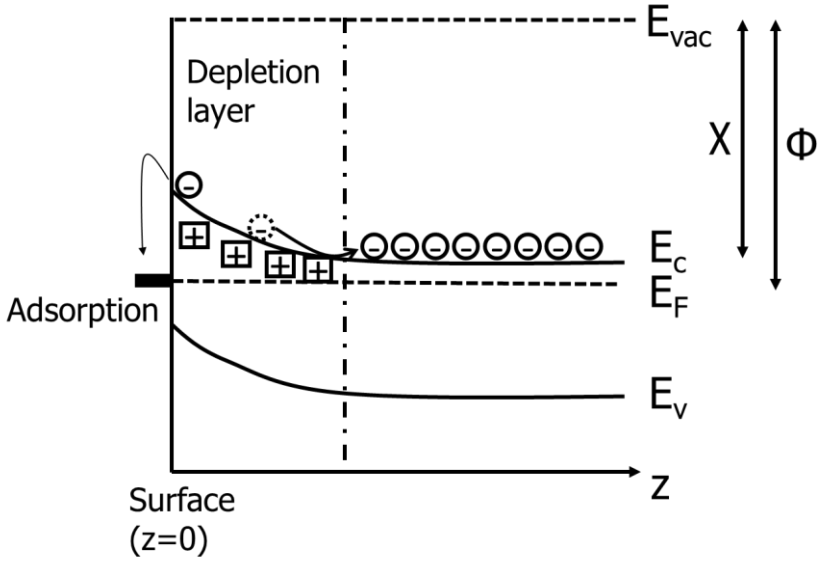

Fig. 1.2 Band bending model illustrating adsorption (ionosorption)

The detection of gas is coordinated by two instants: synthetic gas flow and target gas flow. The synthetic gas is formed with 21% oxygen and the rest is nitrogen. In this case, the surface of metal oxide is filled with negatively adsorbed oxygen that creates high electrical resistance by the electron depletion layer. Ionosorbed oxygen commonly is adsorbed in O^{2-} and O^{-} forms, however, is dependent on temperature and atmosphere humidity [29-31]. When the target gas flows, commonly reducing gas, the ionosorbed oxygen is consumed in a combustion reaction. In this case, the trapped electrons are returned to the conduction band, providing an increase in electrical conductivity. The simple scheme of the gas-sensing mechanism is summarized in Fig. 1.3. The principal figure of merits of the gas sensor is sensor response that is calculated by the ratio of electrical resistance of these two instants: R_a is resistance in synthetic air flow and R_g is resistance in target gas flow, in their steady state ($S=R_a/R_g$).

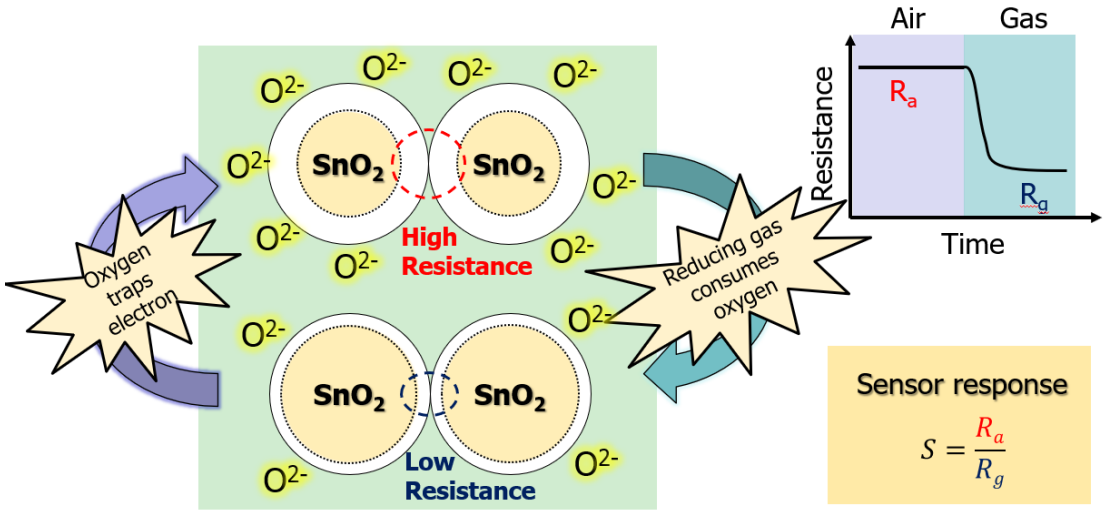

Fig. 1.3 Gas-sensing mechanism of n-type metal oxide semiconductor gas sensors

1.2.4 Adsorption properties on SnO_2

(1) O_2 adsorption

Regarding tin oxide (and other n-type metal oxide semiconductors), the O_2 adsorption properties are among the most important gas sensor factors. As previously mentioned, adsorbed oxygen coordinates the surface carrier density and, eventually, the sensor response. As widely known, oxygen is adsorbed in molecular or ion forms: O_2, O_2^-, O^-, O^{2-}. Yamazoe et al [32] noted these adsorption formats through Temperature Programmed Desorption of O_2 (O_2-TPD) on SnO_2. Fig. 1.5 shows four peaks relative to adsorption properties, named α_1, α_2, β, γ. The desorption α_1 and α_2 occurred at low temperatures, which means they are physically adsorbed. The negatively charged oxygen molecule (O_2^-) has an electron positioned in an anti-bonding orbital that eventually turns more electronically stable than the adsorbed molecule O_2. The chemisorbed oxygen (O^-, O^{2-}) is more predominant in temperatures around 500 °C. Even though Fig. 1.4 shows that β is the O^- desorption peak, there are various studies proposed that O^- and O^{2-} [35-37]. Recently, Suematsu et al [38] determined the O_2 adsorption species by oxygen partial pressure dependence to electrical resistance. The O^- and O^{2-} adsorption species are theoretically represented by equations (1.1) and (1.2), directly proportional to a power of 1/2 and 1/4, respectively [30]. All equations consider sphere shape. R_0 is electrical resistance in a flat band, a is crystallite size, and K_1 and K_2 are adsorption constants.

$$\frac{R}{R_0} = \frac{3}{a}\left(K_1 P_{O_2}\right)^{\frac{1}{2}} + c \qquad (O^- \text{ ads.}) \qquad (1.1)$$

$$\frac{R}{R_0} = \left(\frac{6N_D}{a}\right)^{\frac{1}{2}}\left(K_2 P_{O_2}\right)^{\frac{1}{4}} + c \qquad (O^{2-} \text{ ads.}) \qquad (1.2)$$

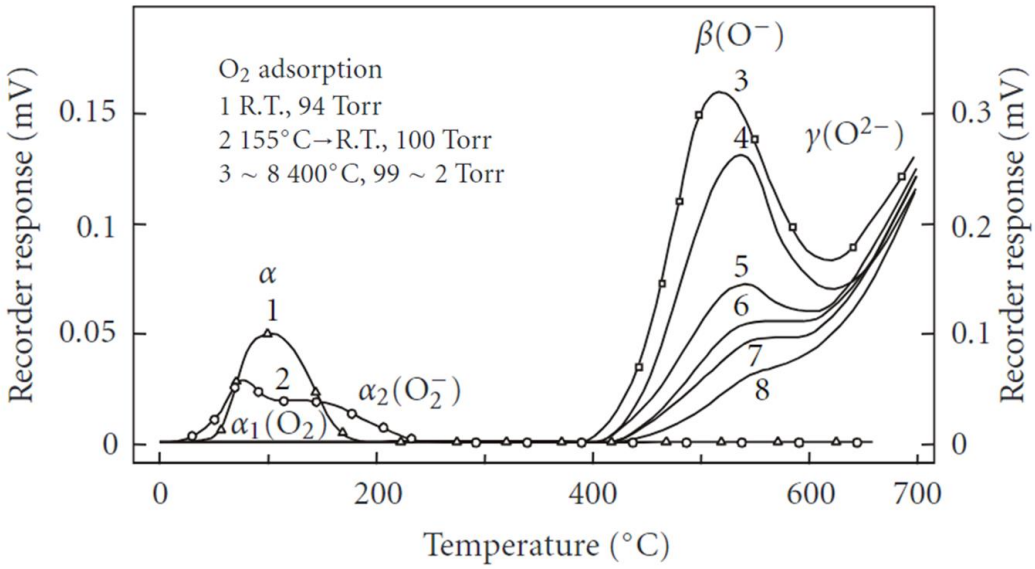

Fig. 1.4 Temperature programmed desorption of SnO_2 to oxygen [32,34]

Sweeping the oxygen partial pressure onto electrical resistance measurement makes it possible to determine the O_2 adsorption species by observing the linearity of the obtained curve at the power of 1/2 and 1/4 of oxygen partial pressure. The electrical resistance measurement is executed to 450°C, 350°C and 300°C (Fig. 1.5).

The main adsorbed oxygen species is O^{2-} for temperatures 350 and 450°C but O^- and O^{2-} competitive adsorption in 300°C owing to non-linearity of $P_{O2}^{1/4}$ resistance curve. The operating temperature of SnO_2 gas sensors is between 200 and 400°C. Therefore, the O^- or O^{2-} are the main oxygen species actuated on the surface as gas detection species. In addition, the γ peak represents lattice oxygen desorption, in other words, is extremely unstable creating abundant oxygen vacancies.

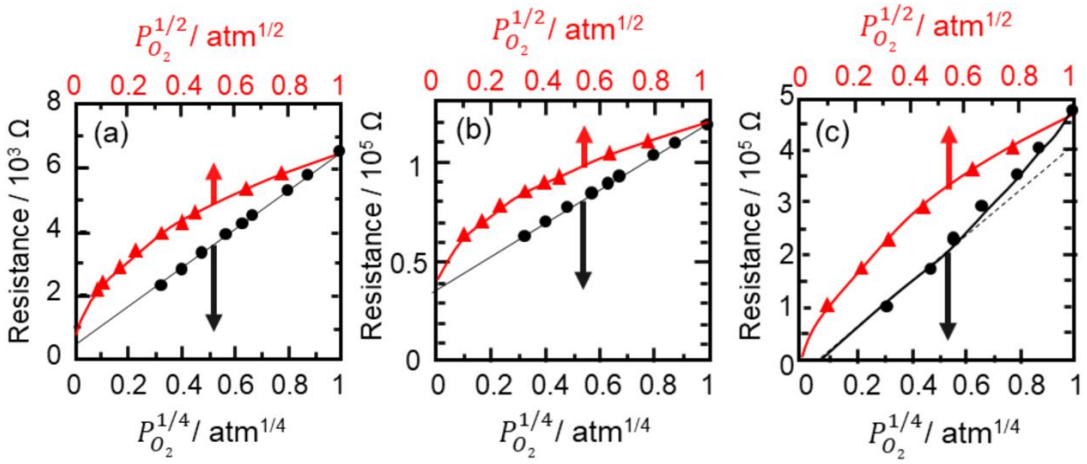

Fig. 1.5 Electrical resistance of SnO_2 varying oxygen partial pressure in 450°C, 350°C, and 300°C [38]

(2) H_2O adsorption

At the laboratory level, the gas sensor measurement and evaluation are realized in extreme conditions, in other words, in a dry atmosphere. Water, however, is an omnipresent element in the air. Hence, it is important to mention the water adsorption effect on electrical resistance or surface charge density. In the same article, Yamazoe et al. show the H_2O-TPD chromatograms with electric conductivity changes [32] (Fig. 1.6). There are two peaks, around 100°C and around 400°C. Among them, the high temperatures adsorb are more related to electrical resistance. The low-temperature desorption is related to H_2O

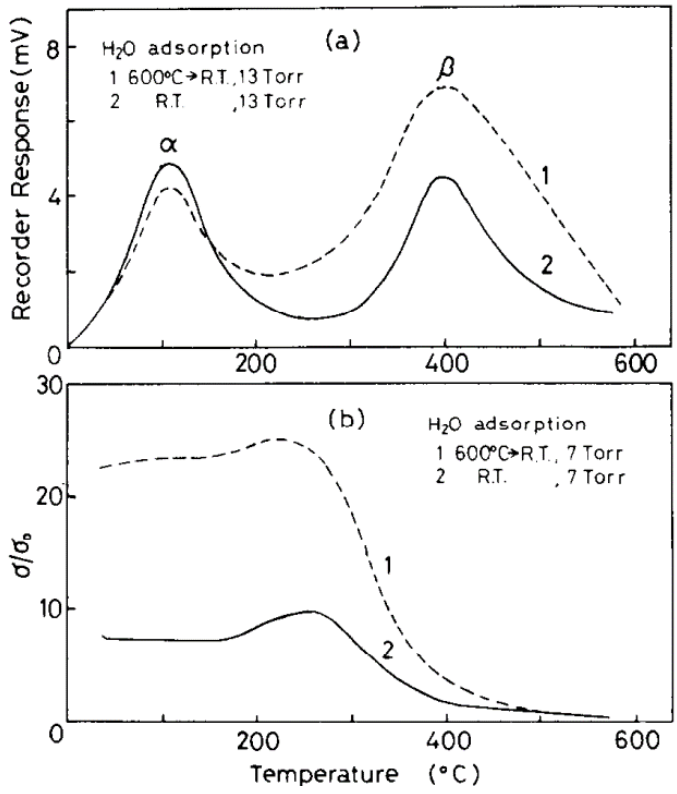

Fig. 1.6 Temperature programmed desorption to water and conductivity results [32]

molecule desorption. These molecules are adsorbed on hydroxyls or on-site of Lewis acid. On the other hand, the high temperatures adsorb are related to hydroxyls, the chemisorbed water [39]. Kohl [40] proposed that water is chemisorbed in a tin or oxygen lattice. Suematsu et al. [29,31,41] proposed that water also adsorbs on adsorbed oxygen, generating hydroxyl. OH^- groups (on tin and oxygen lattice site) completely block the O^{2-} adsorption, leading to O^- species dominantly adsorbed on the SnO_2 surface. That is the main cause that in the wet atmosphere the sensor response is lower than in the dry atmosphere. In actual application, wet effect inhibitors such as Pd and Sb are used to avoid the water adsorption process on the tin dioxide surface [42,43].

(3) H_2 adsorption

SnO_2 gas sensors are appropriate for detecting flammable gases because of their high sensitivity. Among all of them, it considers that H_2 and CO are simple gases to explain the surface mechanism related to electrochemical phenomena.

Fig. 1.7 shows the H_2-TPD chromatograph on SnO_2 [32]. The TPD curve varies depending on the temperature of the H_2 flow introduction. At RT introduction, the H_2 is desorbed completely under 200°C. Therefore, the H_2 adsorption effect on the surface is negligible in terms of gas-sensing. However, at 200°C H_2 flow introduction, shows derived peaks at 220 and 400°C, indicating that H_2 generates H_2O that causes a low sensor response, as explained in the previous subtopic.

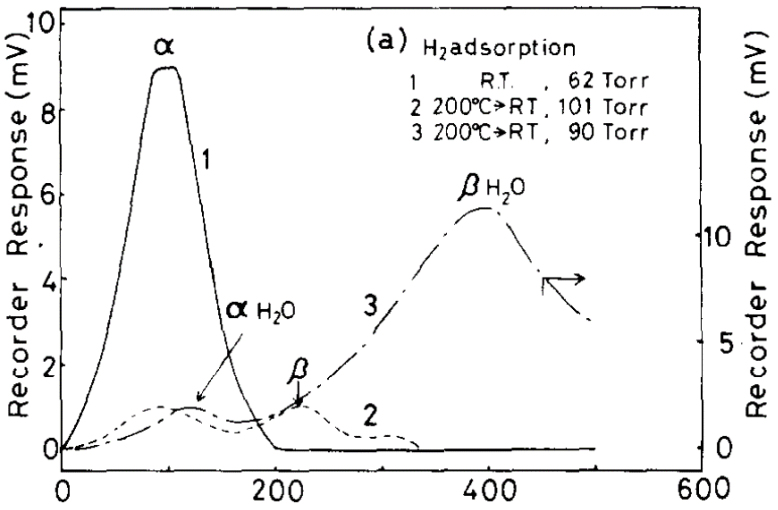

Fig. 1.7 Temperature programmed desorption of SnO_2 to hydrogen [32]

(4) CO adsorption

CO is also a simple gas studied by the gas sensor to explain the fundamental gas-sensing theory. Fig. 1.8 shows the CO-TPD chromatograph [33]. The curves a and b illustrate the desorption without CO introduction. The curves c and d are desorption after CO introduction and e is after CO_2 introduction. There are peaks out of operating temperatures, with a 220°C mean the CO_2 desorption and a 550°C mean the O_2 desorption. Thus, the CO adsorption is irreversible with desorption realized in CO_2 gas form. The CO_2 desorption of TPD in case of CO_2 gas introduction is completed in temperatures lower than 200 °C. Therefore, the CO gas adsorbs on the oxygen site to oxidize.

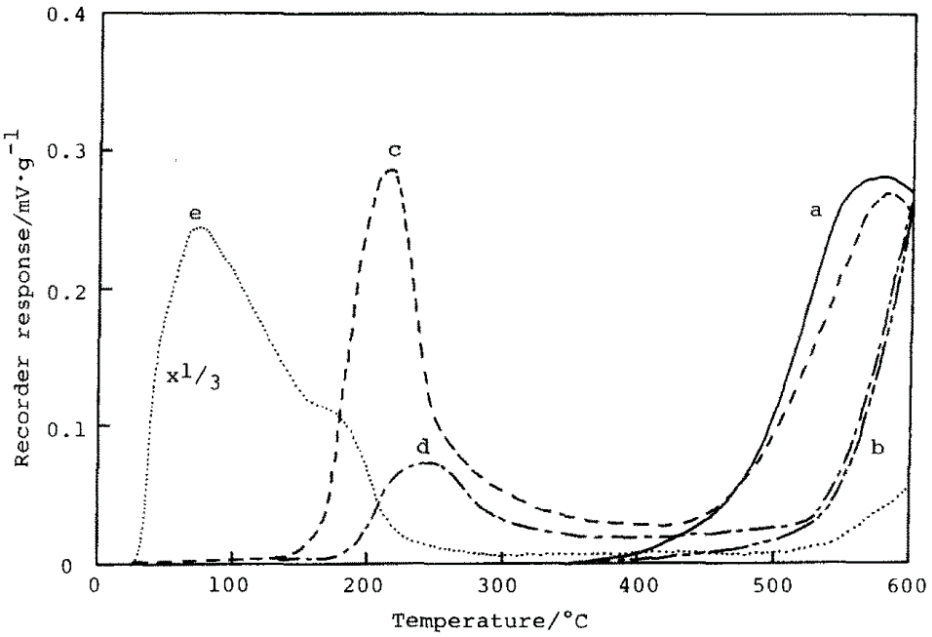

Fig. 1.8 Temperature programmed desorption of SnO_2 to CO and CO_2 [33]

1.3 Key factors design of metal oxide semiconductor gas sensors

The metal oxide semiconductor gas sensor is thermally and chemically stable against various reducing (oxidizing) gases, which possible to detect extremely low concentrations. There are three main key factors in designing highly sensitive semiconductor gas sensors: (a) Receptor function, (b) Transducer function, and (c) Utility factor, as shown in Fig. 1.9 [44]. The receptor function is the electrochemical process that consumes adsorbed oxygen and alters the depletion layer depths. Such function is accentuated through foreign receptors. The transducer function follows the receptor function, which is an integrally electronic process that transduces the charge transfer to electric conductivity. Related to nanomaterial, these processes might be related to tunneling or the Schottky barrier model. The last one, the utility factor is related to gas diffusion, and the reaction occurred effectively, which is associated with Knudsen diffusion. Its function is strongly dependent on the morphology of the sensing layer.

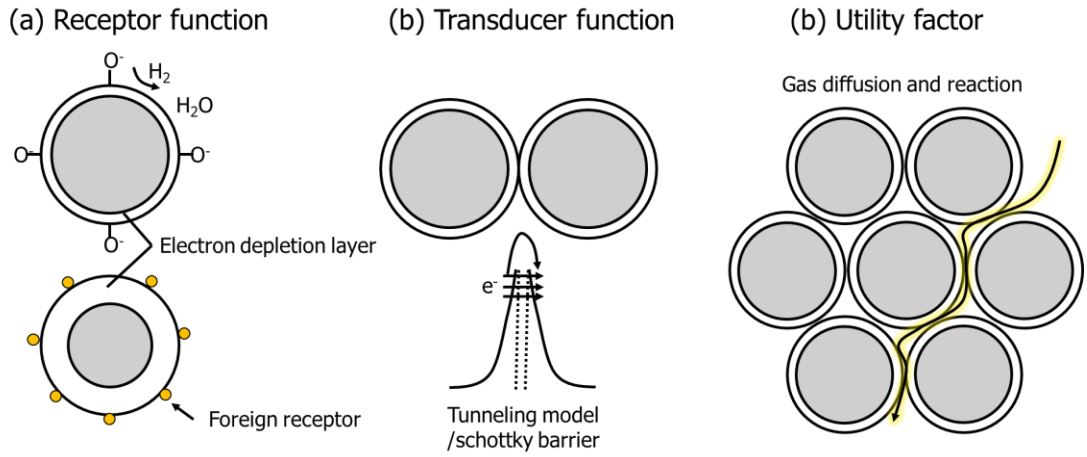

Fig. 1.9 Three main factors for designing metal oxide semiconductor gas sensors.

1.3.1 Receptor function

The additives to enhance the sensitivity of metal oxide semiconductor gas sensors are noble metals and metal oxides. Fig. 1.10 shows the sensitivity for noble metal-loaded tin dioxide [45,46]. The sensitivity, or well-known sensor response, is higher for loaded SnO_2 than neat SnO_2. Moreover, the high sensor response peak is shifted to low temperatures. Hence, the noble metal might act catalytically reducing the enthalpy energy.

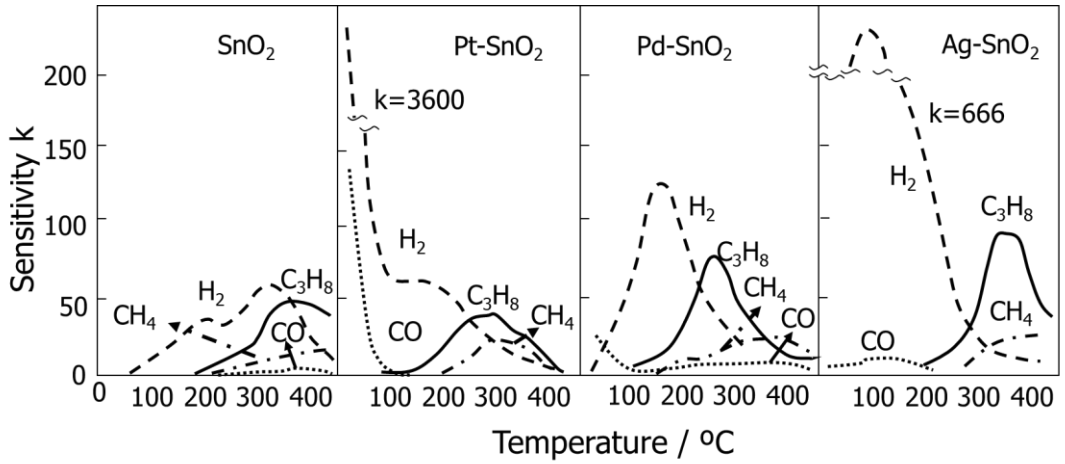

Fig. 1.10 Sensitivity k of noble metal loaded SnO_2.

Fig. 1.11 shows the noble metal on SnO_2 has a lower temperature conversion of toluene and hydrogen than neat SnO_2. The correlation of temperature of 50% conversion of toluene and hydrogen oxidation and temperature of maximum sensitivity is high enough to induce that catalytic oxidation has a relationship with sensitivity enhancement. Thus, the foreign receptor affects the sensitization of the gas sensor. The relation of surface oxidation promoted by foreign reception and the electric conductivity is explained by two mechanisms: (1) electronic sensitization and (2) chemical sensitization.

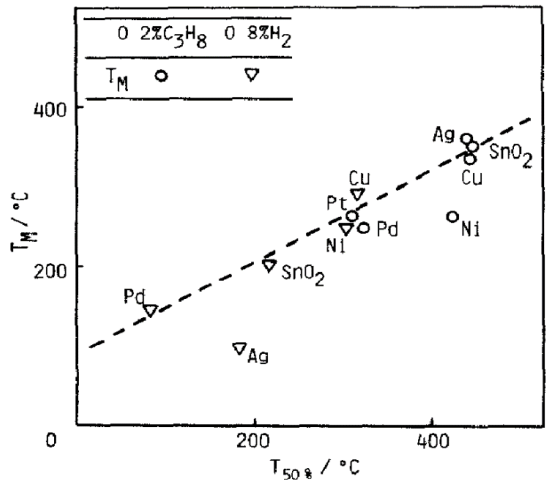

Fig. 1.11 Relationship of 50% conversion of toluene and hydrogen oxidation and their maximum sensitivity [46]

(1) Electronic sensitization

The ionosorbed oxygen formed at operating temperature creates a space charge layer at the surface of SnO_2. The flammable gas such as H_2 consumes the ionosorbed oxygen from SnO2 releasing back the trapped electron. Noble metals such as Pd usually is oxidized in air at operating temperature (Fig. 1.12). PdO (p-type) has a large work function that causes charge transfer from SnO_2 (n-type) to PdO (p-n junction). In equilibrium, the space charge layer is locally increased promoting high electrical resistance [47]. The PdO shifts to Pd metal in reducing ambient, undoing the p-n junction. The trapped electron from SnO_2 is returned and the space charge layer is decreased, providing relatively low electrical resistance. Therefore, the sensor response is increased by an increased space charge layer in air related to Pd redox properties in operating temperature [48].

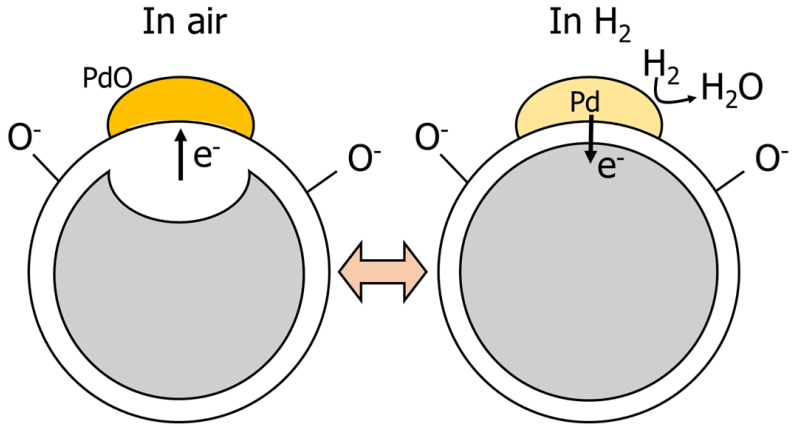

Fig. 1.12 Electronic sensitization mechanism

(2) Chemical sensitization

The spill-over effect is the chemical mechanism that predominantly occurs when noble metal is loaded with metal oxide. For example, the Pt facilitates the adsorption of target gas in its own body, activating and transferring to support material [49,50]. This catalytic process is chemical sensitization promoted by the noble metal receptors. However, it is needed to consider the loading concentration that in some cases the noble metal hinders the oxygen adsorption site, which decreases the sensor response.

1.3.2 Transducer function

The transducer function explains free electron charge density and its moving mechanism toward the sensitive material. One easy approach to varying the donor density is the grain size control. Fig. 1.13 shows the grain size dependent on electrical resistance and eventually on sensor response [51]. The crystallite size D higher than 2L (critical point) is an almost constant electrical resistance to both gases. However, the electrical resistance abruptly increases when D is lower than 2L. The 2L value depends on space charge layer depths. In SnO_2, the space charge layer has 3 nm at 300 °C, thus 2L is 6 nm [51, 53].

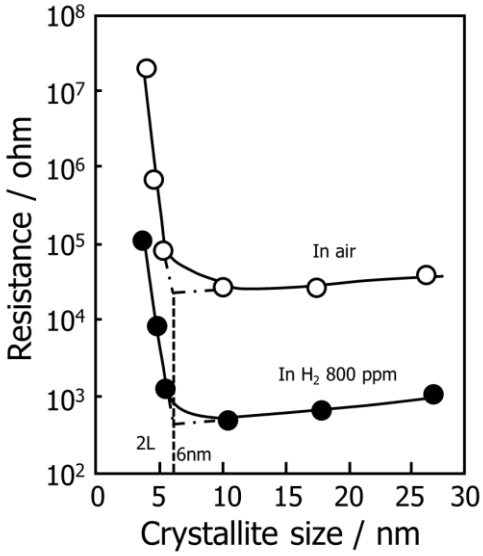

Fig. 1.13 Influence of SnO_2 grain size on electrical resistance in air and in 800ppm H_2

There are three states: (1) D >> 2L, grain boundary control, (2) D ≥ 2L, neck control, and (3) D < 2L, grain control. When the crystallite size is significantly larger than the critical length, the inter-particle contact and particle surface will have high resistivity, becoming the dominant resistive component (grain boundary control). When D becomes comparable with 2L but even higher, the neck component creates a tiny conduction band that becomes dominant to electrical resistance and eventually to sensor response. As the crystallite size is smaller than the critical length, the whole grain of material becomes filled by the space charge layer (grain control). At grain control, the band bending is flat. These phenomena are explained by Yamazoe et al. [54] that the electrical conductivity of grain boundaries (D >> 2L) is influenced by the Schottky barrier and the tunneling effect.

The electrical resistance of semiconductor gas sensors is described by the power law of target gas partial pressure, explored in equation (1.3).

$$R = A \cdot P^{\alpha} \rightarrow \log R = A + \alpha \log P \qquad (1.3)$$

The constant α depends on the material and target gas. For SnO_2 in O_2 gas, the α is 0.5 [55]. Theoretically, this constant explains the relationship between gas adsorption (or reaction) and variation in surface potential. Combined with grain size, the space charge layer theory can be updated. Fig. 1.14 shows the surface potential variated by oxygen partial pressure. Diagrams (a) and (c) are for large particles, and (b) and (d) are for small particles. When partial pressure is low (P_{O2}(I)), the space charge layer is formed near the surface. Increasing the oxygen partial pressure enlarges the depletion region, extending it to the center of the grain (P_{O2}(II)). For small particles, the oxygen partial pressure value for achieving the depletion region in whole grain is much lower than for large particles. Smalling more and increasing the oxygen partial pressure, even if the entire material is in an electron depletion region, the resistance, and the sensor response turned higher. This is because the Fermi level was changed, caused by electron transference from bulk. The shift is theoretically with *p*kT value. This is called volume depletion.

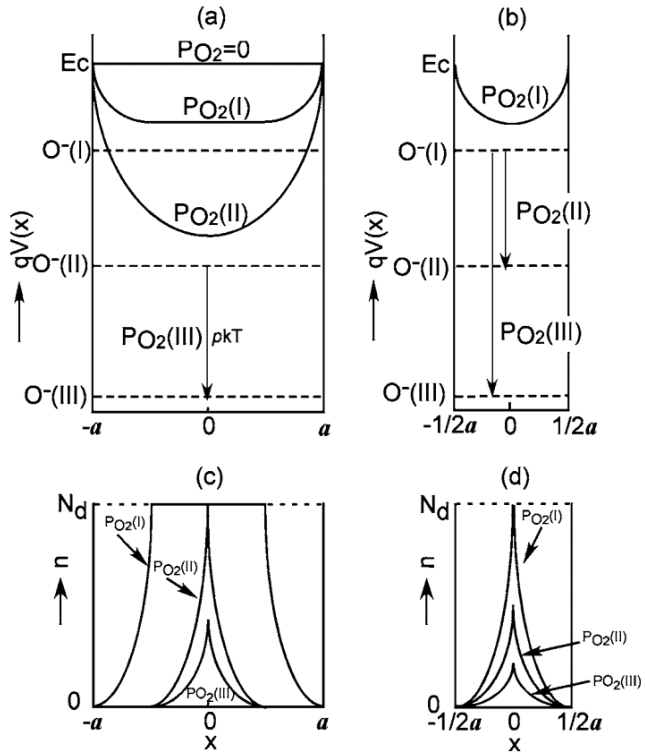

Fig. 1.14 Band energy (a,b) and potential energy profile (c,d) [54].

The following equations consider spherical SnO_2. Before volume depletion, when the depletion layer is not in the center, it's called regional depletion. The electrical resistance in this state is represented by equation (1.4).

$$\frac{R}{R_0} = \exp\left(\frac{m^2}{2}\right) \tag{1.4}$$

The m is related to depletion depths and R_0 is related to the resistance in flat band. On the other hand, the electrical resistance in volume depletion is expressed by the following equations.

$$O_2 + 2e^- \underset{k_2}{\overset{k_1}{\rightleftarrows}} 2O^- \tag{R1.1}$$

$$\frac{R}{R_0} = \left(\frac{3}{a}\right)\left(K_{1,O_2}P_{O_2}\right)^{1/2} + c \tag{1.5}$$

$$O_2 + 4e^- \underset{k_2}{\overset{k_1}{\rightleftarrows}} 2O^{2-} \tag{R1.2}$$

$$\frac{R}{R_0} = \left(\frac{6N_D}{a}\right)\left(K_{2,O_2}P_{O_2}\right)^{1/4} + c` \tag{1.6}$$

Here a is the grain radius, N_d is the donor density, and K is the adsorption equilibrium constant.

The theoretical gas sensor response for hydrogen was summarized in the following equations.

$$\frac{R_a}{R_g} = \left(\frac{3c}{aN_D}\right)^{1/2} P_{H_2}^{1/2} + c \tag{1.7}$$

$$\frac{R_a}{R_g} = f.\left(\frac{3(k_2/k_{-1})}{aN_D}\right)^{1/2} P_{H_2}^{1/2} + c \tag{1.8}$$

Here R_a and R_g are electrical resistance in air and hydrogen gas, k_2 and k_{-1} are the constants of the forward and reverse reaction of R1.2, P_{H2} is hydrogen partial pressure and f is the amplifying factor. Thus, the donor density variated by grain size oxygen partial pressure affects the electrical resistance and the sensor response. Fig. 1.15 summarizes the control of the space charge layer by oxygen partial pressure and grain size.

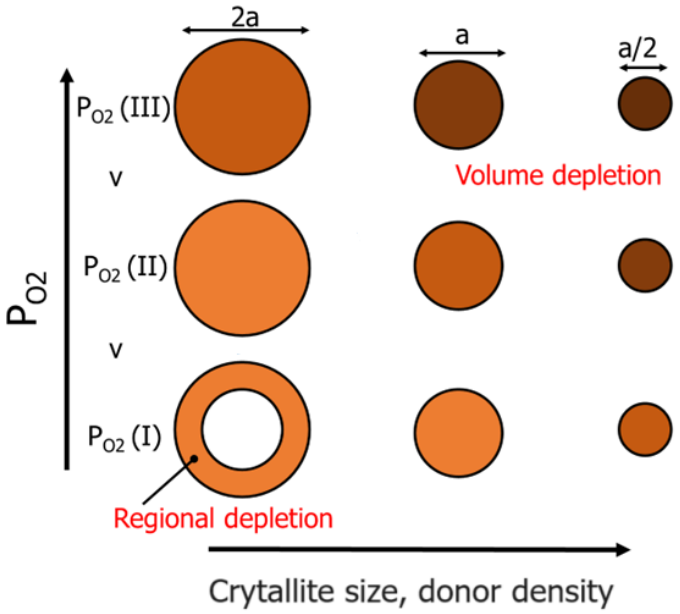

Fig. 1.15 Space charge layer modification on spherical particle

1.3.3 Utility factor

The phenomenon of gas diffusivity in the sensitive membrane is studied at the end of the 20th century [56-58]. Even though the calcination of SnO_2 is operated at 600ºC, the crystallite size is not extremely large, possessing 10-20 nm. This material is considered mesoporous, where Knudsen diffusion predominantly occurs. The Knudsen diffusion is expressed in equation 1.9.

$$D_k = \frac{4r}{3}\left(\frac{2RT}{\pi M}\right)^{1/2} \tag{1.9}$$

Here, the Knudsen diffusion is squarely and inversely proportional to molar mass. Matsunaga et al. [56] studied the gas diffusivity on thin film regarding thickness. The gas concentration of thickness dependence is shown in equation 1.10.

$$C = C_s \frac{\cosh\left\{(L-x)\left(\frac{k}{D_k}\right)^{\frac{1}{2}}\right\}}{\cosh\left\{L\left(\frac{k}{D_k}\right)^{\frac{1}{2}}\right\}} \tag{1.10}$$

Here, the boundary conditions are $C=C_s$ at x=0 and dC/dx=0 at x=L, and k is the reaction rate constant. When the ratio k/D_k is higher, gas penetration into the sensitive membrane is harder. This corresponds to active gas reaction increasing the amount of reacted gas. Moreover, lower Knudsen diffusivity makes it difficult for gas to diffuse into the material. Fig. 1.16 shows the graph representation of eq. 1.10. Here $m = L (k/D_k)^{1/2}$. For a high m value, the high amount of gas reacts on the surface of the sensitive membrane, making it difficult for the gas to diffuse at near electrode space.

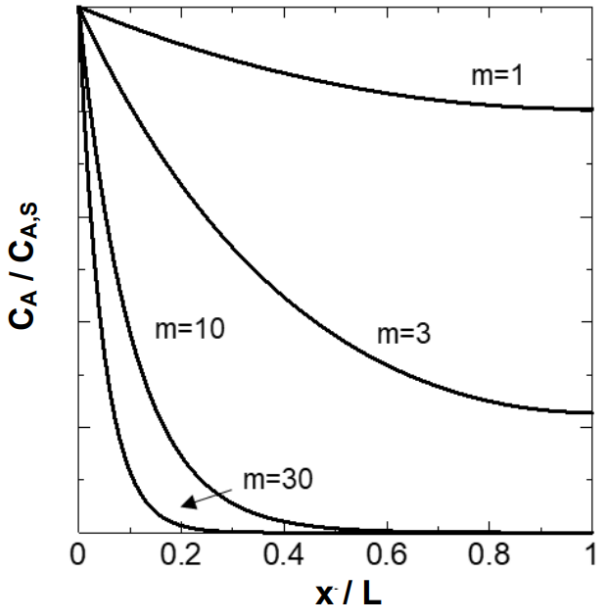

Fig. 1.16 Gas concentration in a porous sensitive membrane [57]

Fig. 1.17 shows the sensor response varying the thickness of the sensitive membrane of the gas sensor. The volcano plot of all thicknesses is explained by the utility factor (eq. 1.10). At low temperatures, the sensor response is predominantly governed by the reaction rate. Conversely, at high temperatures, the sensor response is predominantly influenced by gas diffusivity. This utility factor effect was also recently studied by Kida et al. [60-61], which suggested that a pore size of about 20-30 nm is highly effective against sensor response.

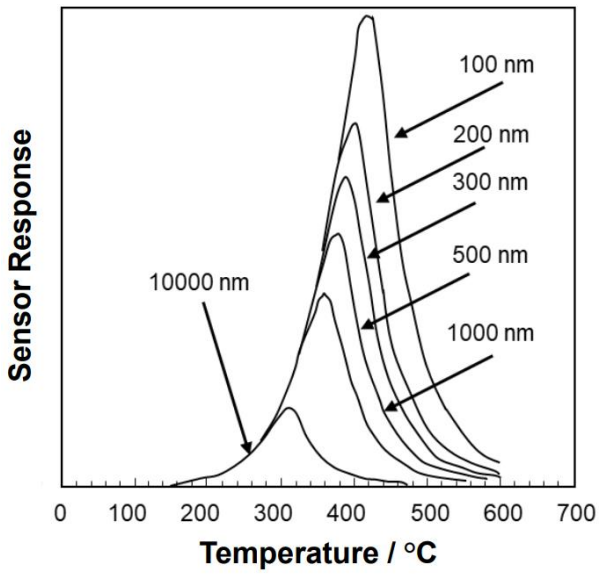

Fig. 1.17 Thickness dependence of sensor response [59].

1.4 MEMS gas sensors

Sensitive membranes, substrates, and heaters constitute gas sensors. Shallow energy consumption is required in IoT applications, in other words, the heater must be a highly effective device or simply miniaturized. Micro electro-mechanical systems (MEMS) overcome all requirements for highly sophisticated use. Generally, MEMS is constituted by sensors and actuators. For the MEMS gas sensors, the heater is the actuator, and the sensitive membrane is the sensor. Besides the microheater that consumes extremely low energy, the miniaturized packaging assists the high-speed sensor response and facilitates the incorporation into portable or wearable devices.

With the micro gas sensors evolution, the application to the trillion gas sensors project has become a reality. However, the application of gas sensors in this device is limited to air quality monitoring. Therefore, it does not require additional technology beyond miniaturization. There is a lot of research about the swarm of smart gas sensors that analyzes the data obtained by tons of sensors and creates new information. Generally, the analysis uses online Machine Learning or Support Vector Machine [62,63].

1.4.1 A highly sophisticated approach – Pulse-driven temperature modulation

Conventional gas sensors are not appropriate for portable devices because of size and energy consumption. MEMS gas sensors are around 1 cm in size, but the sensor membrane is 100 µm squared, with an energy consumption of a few hundred microwatts (Fig. 1.18).

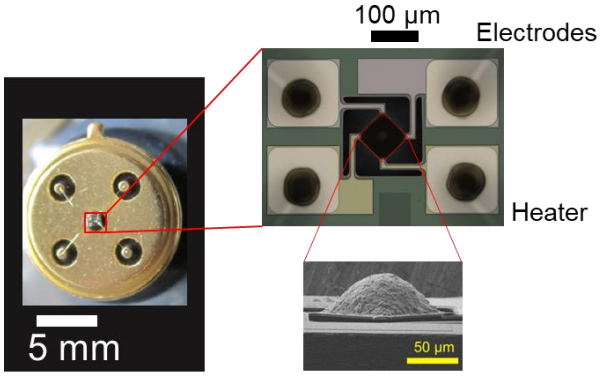

Fig. 1.18 MEMS gas sensor

Fig. 1.18 shows the MEMS gas sensor fabricated by Figaro Engineering Inc. The conventional gas sensor, for example, TGS2600 [64] has 15 times in size. The air bridge structure in electrodes avoids the effect of thermal expansion [65]. Thanks to the size, the thermal capability is stupidly lower, and the total time to rising temperature is shorted to a few milliseconds [65]. When it comes to energy consumption, the pulse-driven mode helps reduce the average power supply through fine duty-cycling.

A highly sophisticated use has been proposed since the start of the 21st century: non-invasive medical diagnosis. By analyzing exhaled gas or skin gas, it is possible to determine if the patient has cancer [66-68] or also analyzing the metabolism [69]. Unfortunately, the current cancer diagnosis is often later. Hence, this non-invasive medical diagnosis is important to early detection of cancer. If the technology applied to identify the gas is in simple access to all smartphone users, the detection will be easier and early. Both material science and data analysis are important to realize this highly sophisticated use.

In addition to the three key factors, MEMS technology with temperature modulation is also an important factor in a high-performance gas sensor. The temperature modulation approach has been studied a lot since the 70s [70-72]. Suematsu et. al. [73,74] proposed a pulse-driven method altering the temperature for each cycle, called a double-pulse drive. These adsorption combustion gas sensors are discussed by Hyodo et. al [75,76]. As shown in Fig. 1.19, (1) the gas is diffused into the sensitive membrane at low temperatures, which increases the gas concentration at the near electrode region. (2) The heater is rapidly on, where occurs the gas reaction abundantly, returning to (1) to adsorb more gas.

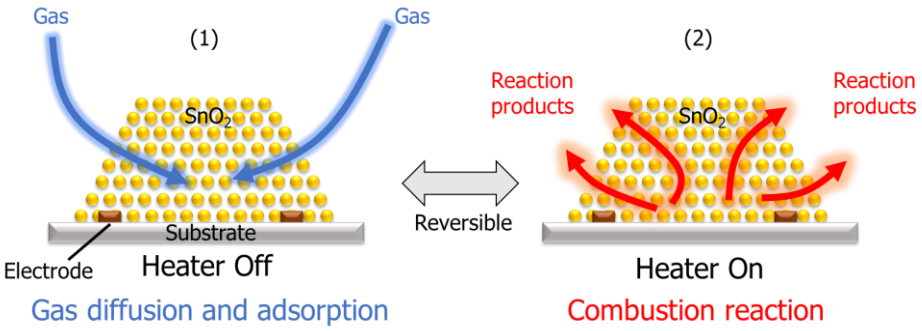

Fig. 1.19 Gas diffusion and reaction on the gas sensor

1.5 Motivation

Tin dioxide is widely utilized in gas sensors due to its high sensitivity to combustible gases. Incorporating metal or metal oxide on the surface, modulation of donor density through nanoparticle size control, and Knudsen diffusion into mesopores influence the sensor response significantly. The pulse-driven method utilizes the latter approach at the micro gas sensor (MEMS gas sensor). However, the pores within the deposited sample, and the number of contacts between particles and electrodes can also critically impact the sensor response. The wider distribution of agglomerated particles, ranging from 100 nm to 100 μm, exacerbates these effects on sensor device production, especially impacting micro gas sensors. The micro gas sensors have 1-5 μm of electrode distance thus the secondary particles with 10 μm or larger could cause high resistance and low gas-sensing performance. The Knudsen diffusion length is limited to approximately 1 μm, for that reason, almost all primary particles of coarse secondary particles are not influenced by gas reduction, which decreases the sensor response. Therefore, this research proposes studying the relatively narrow distribution of tin dioxide through size-based classification, potentially mitigating the mentioned adverse effects. Furthermore, the classification process can distinguish narrow distributions with differing peak positions, enabling assessing how agglomeration size affects the gas sensors.

Chapter 2 outlines the preparation of sensor materials, fabrication of sensor devices, and gas sensor response measurement. Chapter 3 details the classification method for producing sub-micron and micron-sized secondary particles, along with fundamental sample evaluation. Chapter 4 elaborates on the electrical and chemical characterization of sub-micron and micron-sized agglomerations, focusing on sensor device applications to verify the size effect on electrical resistance and CO catalytic combustion for surface reaction. Chapter 5 describes the electrical and gas-sensing properties of the Pd-loaded classified SnO_2 to confirm the size effect on Pd-loading. The conclusion includes summaries and acknowledgments.

2. Experiments

2.1 Introduction
2.2 Sample synthesis
2.2.1 Synthesis of SnO_2 nanoparticles
2.2.2 Classification of SnO_2
2.2.3 Synthesis of Pd-SnO_2 nanoparticles
2.3 Material evaluation
2.3.1 Crystal structure
2.3.2 Morphology observation
2.3.3 Pore properties and specific surface area
2.3.4 Particle size distribution
2.3.5 Catalytical evaluation
2.4 Manufacturing of sensor element
2.5 Sensor measurement system
2.5.1 Resistance measurement system
2.5.2 Evaluation of sensor performance

2.1 Introduction

This chapter presents the synthesis method of neat SnO_2 and Pd-loaded SnO_2. The SnO_2 is prepared by precipitation using chloride-based tin precursor ($SnCl_4$) and ammonium solution. The precipitated $Sn(OH)_4$ is dried and calcined for sensor usage. However, as mentioned in the motivation, the conventionally synthesized SnO_2 has a variety of secondary particle sizes. Therefore, the particle-size classification is applied to mitigate the irregularly large particle effect and clarify the impact of different secondary particle sizes on electrical and gas-sensing properties (Chapters 3 and 4). The classification is executed by the sedimentation method. The Pd-loaded SnO_2 is prepared to 2 mol% Pd by impregnation with Pd nitrate precursor. In addition, the characterization of the prepared sample and sensor measurement method are described. The chemicals used in SnO_2 synthesis and sensor element manufacturing are shown in Table 2.1.

Table 2.1 Chemicals used in SnO_2 synthesis and sensor element manufacturing.

Chemicals	Chemical formula	Purity /%	Chemical company
Tin chloride pentahydrate	$SnCl{\cdot}5H_2O$	98	Fujifilm Wako Pure Chemical Corporation
Ammonium hydrogencarbonate	NH_4HCO_3	20 – 23 (as NH_3)	Fujifilm Wako Pure Chemical Corporation
Ammonium nitrate	NH_4NO_3	98	Fujifilm Wako Pure Chemical Corporation
Dinitro Diamine Palladium (II)	$Pd(NO_2)_2(NH_3)_2$	-	Tanaka Precious Metals K. K.
Glycerin	$C_3H_8O_3$	99.5	Fujifilm Wako Pure Chemical Corporation

2.2 Samples synthesis

2.2.1 Synthesis of SnO_2 nanoparticles

The flowchart of the tin dioxide synthesis is shown in Fig. 2.1. The stannic acid ($SnO_2{\cdot}nH_2O$) is prepared by hydrolysis of Tin (IV) chloride pentahydrate ($SnCl_4{\cdot}5H_2O$; 1M) dropwise into ammonium hydrogencarbonate (NH_4HCO_3; 1M), with a mass ratio of

1:5, respectively. Afterward, the precipitated stannic acid is washed by centrifugation with ammonium nitrate (NH_4NO_3) solution to remove Cl^-. The centrifugation is configured to 3500 x g, 10 min, 15°C, operating 10 times. The rest of NH_4NO_3 in the washed gel is removed by high-speed centrifugation (12000 x g, 10 min, 15°C) and dispersed into de-ionized water. The completely washed gel has a white color with some impurities. Thus, the impurities are removed by separating the funnel or filter. The obtained gel is dispersed again in de-ionized water and dried at 60°C (or low temperature) for 12h in a hotplate and vacuum dryer. This temperature is important to avoid unnecessary larger agglomeration formation. The dried powder is ground and calcined to 600°C for 3h. The ambient condition of calcination is O_2 [41, 61]. The calcined powder is ground, obtaining the SnO_2 nanoparticle powders. The conventional method operated commonly in this lab is hydrothermal treatment. However, the hydrothermal treatment creates hard nuclei that promote crystal growth with 100 μm order sizes during drying. The comparison of current synthesis and hydrothermally synthesized is discussed in Chapter. 3.

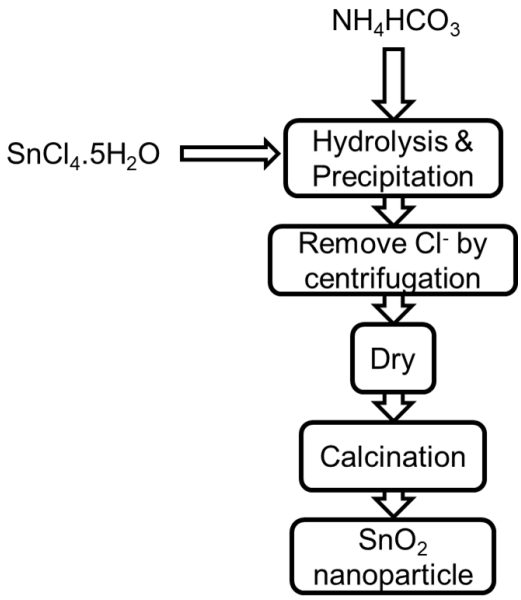

Fig. 2.1 Flowchart of SnO_2 nanoparticle synthesis

2.2.2 Classification of SnO_2

The electrical resistance and sensor response might be dependent on secondary particle size. In discussing this view, it must be synthesized SnO_2 with different secondary particles with narrow particle size distribution. There is little research [77,78] investigating the micro-size particle effect on gas sensors, however, all of them create the sample in another way that does not ensure that the material has the same intrinsic electrical or sensor properties. To guarantee that the electrical properties are preserved, the SnO_2 with controlled secondary particle size is created using a simple sedimentation method that does not involve chemical procedures. Fig. 2.2 shows the flowchart of SnO_2 classification. SnO_2 powder is mixed into de-ionized water for a few minutes in a centrifuge tube. After waiting 1 min at rest, the tremendously large particle (10-100 μm) is precipitated and removed. This large particle is considered the irregular component in a sensitive membrane, which produces low electrical and gas-sensing reproducibility. The supernatant suspension is submitted in low-speed centrifugation (500 rpm, 5 min, 15 °C). The obtained supernatant is separated from precipitation and drying each component. This procedure is repeated until the supernatant is completely transparent, or the precipitation is not formed anymore. The supernatant dried powder is called fine SnO_2 (fine secondary particle SnO_2) and precipitated dried powder is called coarse SnO_2.

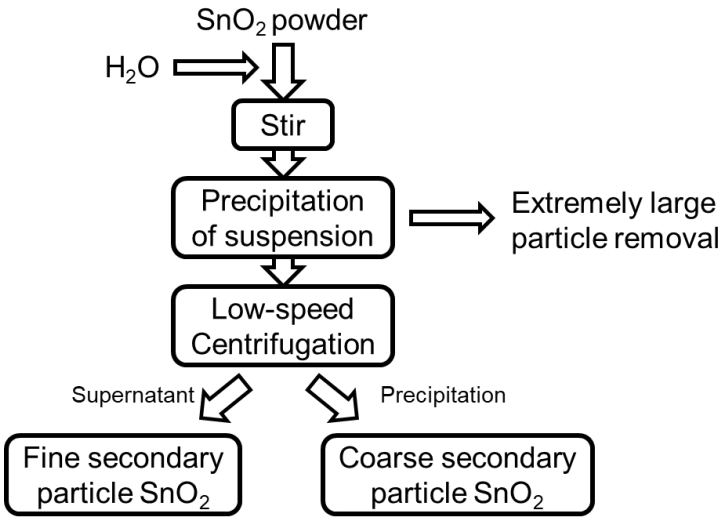

Fig. 2.2 Flowchart of SnO_2 classification

2.2.3 Synthesis of Pd-SnO_2 nanoparticles

The Pd effect on SnO_2 is largely studied, which promotes high sensitivity and avoids water poisoning of the tin dioxide surface. The main proposal in this thesis is the effect of Pd (receptor function in terms of key design factor) on different secondary particle sizes. Therefore, the synthesis method is applied to the classified sample. Pd-SnO_2 is synthesized by the impregnation method with dinitro diamine palladium (II) ($Pd(NO_2)_2(NH_3)_2$). Fig. 2.3 shows the flowchart of Pd-SnO_2 nanoparticle synthesis. First, the classified SnO_2 (1g), ethanol (17.5 mL), and water (7.5 mL) are mixed for 5 min. The stirrer bar needs to be made of glass to avoid the dissolution of bar material (for example, PTFE). The $Pd(NO_2)_2(NH_3)_2$ is added carefully into the mixing solution. The amount of this precursor is calculated to incorporate 2 mol% on SnO_2. For precision and reproducibility, the mixed system is applied vacuum by diaphragm pump. After 1h, the solution is dried at 120 °C for 12h. The dried powder is ground and calcined at 580°C for 3h, in O_2. The temperature needs to be lower than 600°C to avoid exaggerated crystal growth.

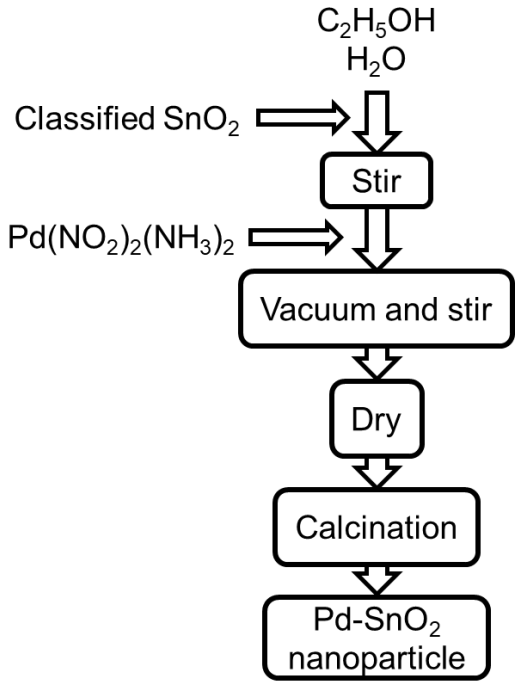

Fig. 2.3 Flowchart of Pd-SnO_2 nanoparticle synthesis

2.3 Material evaluation

2.3.1 Crystal structure

The X-ray diffraction method is simple and direct in confirming the expected synthesis. The results of XRD show the diffraction pattern of the crystal structure, which is like the ID of the material. Referring to databases such as the Inorganic Crystal Structure Database (ICSD), it is possible to assume or deduce the crystal phase and compounds. XRD used is benchtop type (Rigaku Co., Ltd., Mini Flex). The X-ray source is CuKα with 40 kV, 30 mA, the scanning speed is 5.0°/min, the scanning step is 0.02°, and the range is 2θ=20-80°. The crystallite size is calculated by Scherrer's equation, eq. 2.1.

$$D = k\lambda/\beta \cos\theta \tag{2.1}$$

Here, D is crystallite size, k is the constant that represents the particle shape (considering sphere, k=0.9), β is full width at half maximum of the peak (FWHM), λ is the wavelength of CuKa (0.1542 nm), and θ is the center angle of the peak.

The main peaks of SnO_2 are (110), (101), and (211). Therefore, the crystallite size is calculated by averaging these three peaks.

2.3.2 Morphology observation

The micro-size morphology is observed by Scanning Electronic Microscopy (SEM). The machine is JEOL JCM-7000. A carbon tape is attached to the cell holder, and a small amount of sample powder is placed on it. The observation with this low-resolution SEM is important for qualifying the classification method of 2.2.2., in addition to the particle size distribution analysis.

2.3.3 Pore properties and specific surface area

The pore properties such as specific surface area and pore volume are measured by the N_2 adsorption/desorption method (MicrotracBel Corp., BELSORP-mini II). The sample needs to be pretreated to clean the sample surface. The amount of powder depends on porosity. For synthesized SnO_2, 0.25 g is enough. N_2 is adsorbate used, starting at 77

K, and the partial pressure ratio P/P_0 alters from 0 to 1, and then the desorption process also (from 1 to 0). The specific surface area is calculated by the BET method and the pore volume is calculated by the BJH method.

2.3.4 Particle size distribution

With SEM observation, particle size distribution is an important measurement to evaluate the separation method quality (HORIBA, Partica LA-960V2). This machine measures particle size from 10 nm to 5 mm by laser scattering method. The cell is a flow cell, with de-ionized water as solvent. The measurement data is analyzed for volume distribution and number distribution. This research is focused on volume distribution.

2.3.5 Catalytical evaluation

The CO gas chromatography and temperature-programmed-reaction (TPR) are executed to determine the catalytical properties of classified SnO_2 and Pd loading effect (Pfeiffer Vacuum, QMS PrismaPro; J-Science Lab Co. Ltd., GC). Gas chromatography is used to analyze the compounds in the gas phase by analytical separation method using a column oven. The TPR is used to investigate the redox properties and adsorption reactions by measuring the consumption and generation rates of byproducts at continuously increasing temperatures. The detector for TPR is a Quadrupole Mass Spectrometer (QMS). The QMS is more sensitive than gas chromatography, which can detect signal variation that has not been detected in gas chromatography. The detector of gas chromatography is a flame ionization detector (FID). The exhaust gas is sampled every 20 min for gas chromatography and the mass spectrum is always measured. Considering that the mass number *m/z* of CO is equal to N_2 with 28, the system must not include nitrogen for accurate measurement. CO/Ar and O_2/Ar are the gases used for all programmed measurements. The sample (around 0.3 g) is subjected to pressure to make granules. The machine pressure (ϕ40) is 0.3 MPa for 1 min and 4 MPa for 5 min. The disk was made in ϕ10 (effective pressures are: 3.6×10^4 torr for 1 min and 4.8×10^5 torr for 5 min) and broke on the sieve of 250 to 450 μm. Finally, 50 mg is taken to measure of catalyst. The sample is positioned intra-canal by quartz wool, like a conventional catalyst material preparation. The measurement program is summarized in Figure 2.4.

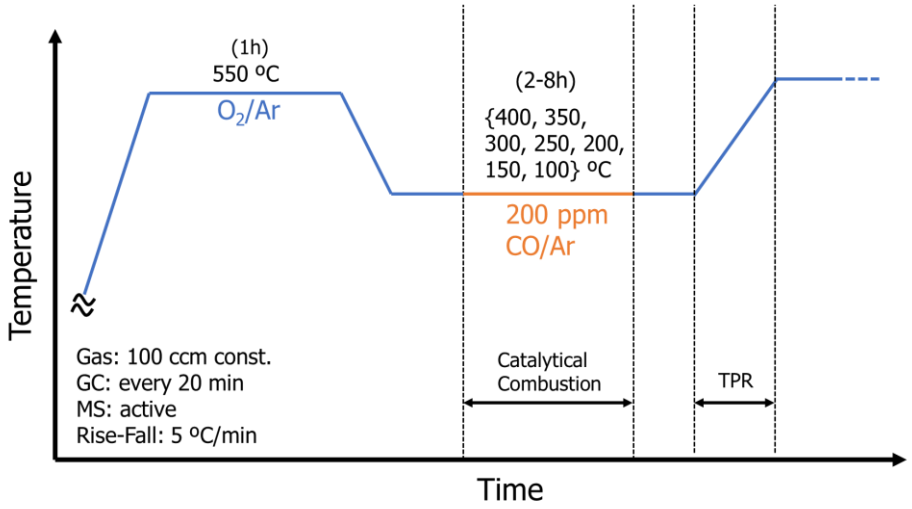

Fig. 2.4 CO-TPR: program

The keeping time (2-8h) is empirically decided when the gas-phase concentration and mass spectrum seem in equilibrium. The mass number *m/z* verified is 17 for water, 28 for CO, and 44 for CO_2. It is important to note that 28 is the fragment ion peak of CO_2 [80], so *m/z* 28 shows the combination of CO and CO_2 behavior. The *m/z* 18 is the real *m/z* of H_2O, however the Ar gas affects the number 18. Therefore, for water or hydroxyl analysis is used *m/z* 17, a fragment peak of water [81]. The refreshment on each measurement (550ºC for 1h) is crucial to conserve the same initial surface condition (until falling temperature). To avoid N_2 and CO mass spectrum interference, the gas line is cleaned by vacuum substitution and heating by heat-gun.

2.4 Manufacturing of sensor element

The micro gas sensor (MEMS gas sensor) is made by the microinjection technique (Eppendolf; FemtoJet 4i). Fig. 2.5 shows the flowchart of sensor device manufacturing. The mass ratio between sample powder and glycerin is 1.5:1. The paste is made in an agate mortar in a controlled manner: 300×clockwise, 300×counterclockwise, 250×vertical, 250×horizontal, again 300×clockwise, 300×counterclockwise, 1 min defoaming treatment, 10×clockwise, in this order. This procedure is exceedingly important to guarantee a minimum reproducibility. The paste is filled into a 50-micrometer capillary tube using capillary action. At this moment, the pressure controller is 0 hPa. The tube is carefully positioned on top of the MEMS gas sensor electrode. The pressure control has two control ways: pressure constant (Pc) and pressure instant (Pi), where the Pc is the pressure that is constantly on, and the Pi is the pressure applied when the pedal is stepped. In the injection procedure, the Pc is adjusted to 20-30 hPa, and the Pi is adjusted to 40-50 hPa. The bit of paste stands out by Pc, and this is carefully touched onto the substrate. With the surface tension, a dome shape on MEMS is formed and rapidly the tube is left away. The thickness of the sensitive membrane is aimed to obtain 30 μm. Afterward, the MEMS gas sensors are vacuum dried in a controlled manner: with no vacuum, 70ºC for 30 min, 100ºC for 30 min, 120ºC for 1h, 150ºC for 1h, 180ºC for 20 min, vacuum is started for 1h and is cooled naturally. The calcination is managed by an onboard microheater, 500ºC for 30 min in synthetic air flow 100 ccm ($mL.min^{-1}$).

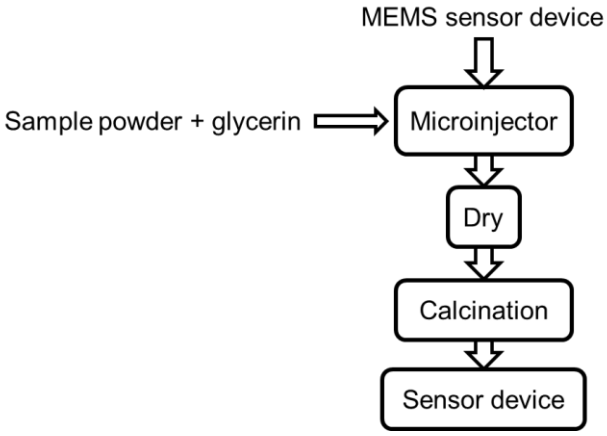

Fig. 2.5 Sensor device manufacturing

2.5 Sensor measurement methods

The electrical resistance of the MEMS gas sensor is measured to evaluate the gas-sensing properties of the separated sample. The data acquisition system (DAQ) is made by Kyushu Keisokki Co., Ltd. The DAQ is constituted by an NI-DAQ device (NI-USB6289) and an analog output module (NI-9263) that is used for heater manipulation. The protection circuit is built in. Fig.2.6 shows the schematic diagram of the MEMS gas sensor measurement. Table 2.2 shows the relationship between heater voltage and temperature.

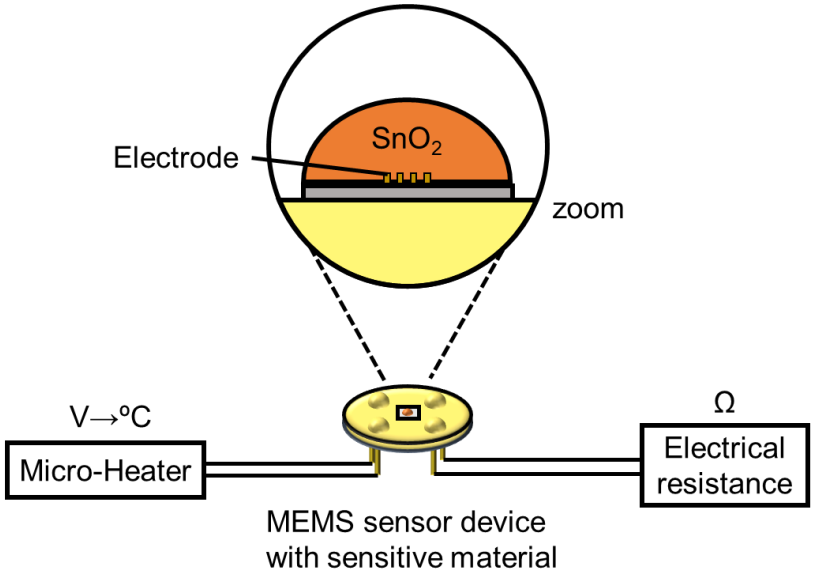

Fig. 2.6 Schematic diagram of MEMS sensor device measurement

Table 2.2 Relationship of heater voltage and temperature

Voltage supply (V)	Heater temperature (ºC)
2.1	500
1.9	450
1.7	400
1.5	350
1.3	300
1.1	250

2.5.1 Resistance measurement system

The prepared micro gas sensors are placed onto a socket in the chamber. The chamber must be made of quartz glass, which resists until 1300ºC (short-term basis). The mass flow is adjusted to 100 ccm constant. The electrical resistance is measured based on a bridge circuit or directly by an electrometer (Keithley 2701). The gas used is N_2, O_2 for carrier gas control, and ethanol, CO, and H_2 for target gas measurement. The N_2 amount adjusts the gas concentration and O_2 is fixed at 21 ccm (always 21%, to avoid the oxygen partial pressure effect). Fig. 2.7 shows the MEMS gas sensor measurement system constituted by a gas flow system (array of kofloc 8700), chamber, data acquisition system, and temperature controller. The measurement is operated automatically. The number of channels is 4 or 12 ch, depending on socket availability and chamber size.

The tuning of temperature and time of pulse-driven mode is hard to operate for multiple samples. This research will be focused on steady-state temperature measurement. However, the dynamics analysis of gas-sensing response will also be discussed briefly. This is because the difference in secondary particle size directly impacts gas diffusivity.

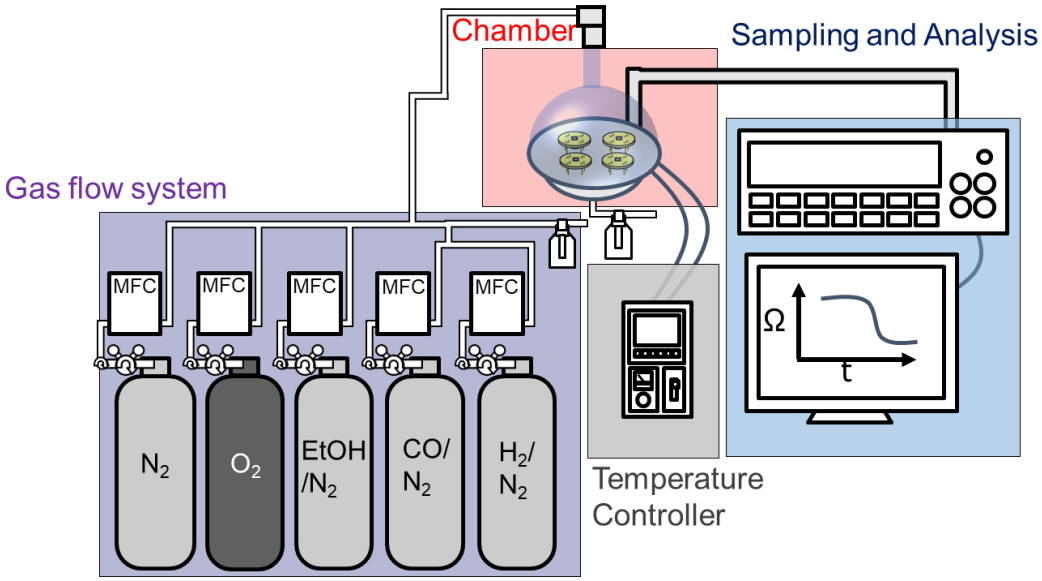

Fig. 2.7 MEMS gas sensor measurement system

2.5.2 Evaluation of sensor performance

Even though the commercial gas sensor is appropriate to use in diverse ambient conditions, the laboratory-made gas sensor is readily poisoned by water and hydrocarbons, mainly at low temperatures. The pretreatment addresses this issue by raising the temperature to 500ºC for 10 minutes, which standardizes the surface electronic states before decreasing to the operating temperature. The operating temperature range is from 200 to 350ºC.

Table 2.3 summarizes the gas sensor measurement condition. The target gas is H_2, CO, and C_2H_5OH. The simple gases H_2 and CO explain the fundamental gas-sensing properties. Ethanol gas is a well-known reaction path and eventually the byproduct species: acetaldehyde, ethylene, acetic acid, and carbon dioxide (complete oxidation).

Table 2.3 Sensor measurement condition

Ambient	Dry
Driven method	Steady-state temperature
Sampling time	5s/12ch
Operating temperatures	200, 250, 300, 350ºC
Preheating temperature	500ºC, 10 min
Target gas	H_2, CO, C_2H_5OH (N_2 base)
Gas concentration	10, 20, 50, 100 ppm

3. Classification of SnO_2 secondary particle

3.1 Introduction

3.2 Classification of hydrothermally synthesized SnO_2 and their limitation

3.3 Characterization of classified SnO_2 – as-synthesized SnO_2

3.4 Characterization of top-down technique to fine-SnO_2

3.5 Summary

3.1 Introduction

In Chapter 1, it was briefly mentioned that tin dioxide synthesized through hydrothermal methods, one of the most used methods for synthesizing this material, results in a wider size distribution of secondary particles. The over 10 μm particles increase the electrical resistance when operating MEMS gas sensors because the electrode distance is in 1μm ordered size. The around 1 um SnO_2 was suggested to overcome the high electrical resistance issue, by creating more contact with electrodes. However, investigating variated tin dioxide micro-size particles on thick film and MEMS sensors is crucial to finding the explanation factor of the secondary particle size effect on gas sensors. This chapter presents the classification method of SnO_2 using a physical separation method coordinated by sedimentation and decantation. First, the classification is applied to hydrothermally synthesized tin dioxide, analyzing the crystal structure and morphology via XRD and SEM. Afterward, the classification of as-synthesized SnO_2 (drying the gel produced in hydrolysis) is executed and analyzed by the same performed characterization. In addition, the particle size distribution was measured by laser scattering to evaluate the separation technique quality and their potential use for micro gas sensors. Furthermore, it investigated a top-down technique to obtain fine particles, in other words, the modification of the drying parameter provides a tin dioxide formed predominantly by fine SnO_2. At the end of this chapter, it clarified which prepared tin dioxide is appropriate for this research.

3.2 Classification of hydrothermally synthesized SnO_2 and their limitation

The uniform primary particle is suggested as an important consideration in gas sensor manufacturing. The contact between two different primary particle sizes provides pinning even though it is a contact between the same material. In reduced states, the Fermi level of SnO_2 is dependent on particle size [82]. At the contact occurs pinning, in other words, a contact potential is generated keeping the Fermi level in equilibrium. Therefore, exceedingly non-uniform tin dioxide affects the electric conductivity. Aiming the

production of uniform SnO_2, hydrothermal treatment is executed on the produced gel by $SnCl_4$ hydrolysis. The uniform or monodispersed SnO_2 is important to obtain controlled primary particle size [83]. Usually, in gas sensors, the nanomaterial has around 15 nm of crystallite and particle size, which eventually creates a considerable volume of mesoporous and spherical shape control. Fig. 3.1 shows the flowchart of hydrothermal synthesis of SnO_2. It is identical to the proposed synthesis in Chapter 2, however, after the washing process in high-speed centrifugation, the precipitated gel is mixed in water once more and pH is adjusted to 10.5 by Tetramethylammonium hydroxide (15% TMAH; Fujifilm Wako Pure Chemical Corporation) solution. The 75×4 (=300) mL of solution is put into four PTFE bottles. The bottles are placed into the autoclaves for hydrothermal treatment at 200ºC for 10 h. The obtained sol is mono-dispersed. They are dried in a rotary evaporator at 60ºC in a diaphragm vacuum pump. Afterward, the partially dried crystal is dried again in a vacuum dryer. The dried sample is ground and calcined at 600ºC for 3h under O_2 flow, obtaining SnO_2 nanoparticles. Fig 3.2 shows the SEM image of hydrothermally synthesized SnO_2 calcined powder. The secondary particles are predominantly of sizes around 10 μm, with some being sub-micron and others around 100 μm. The shape is not uniform; it has a characteristic sharp form. The sharpness may be due to the strong bonding of the crystal being broken. The large secondary particle is formed mainly during the drying process. The mono-dispersed sol has tin ions (Sn^{4+}) dissolved into it, which when dry ions are deposited onto nuclei or primary particles, in the final drying process the contact between particles turns stronger, creating the irreducibly large particle. Moreover, the intrinsic concentration of SnO_2 on monodispersed sol arguably can drive the large particle [84]. The bonding is strong above unbreakable even in the ultrasonication process. On the other hand, the sub-micron secondary particle is formed and glued on large particles with water capillary force (electrostatic OH contact). These easily can detach from large ones with ultrasonication. In the case of accessible secondary particle size production, the bottom-up process – ball-milling - is suggested to overcome it. However, the intra-secondary particles can be formed with another generating process. So, the bottom-up process is avoided to not produce an extra considerable parameter.

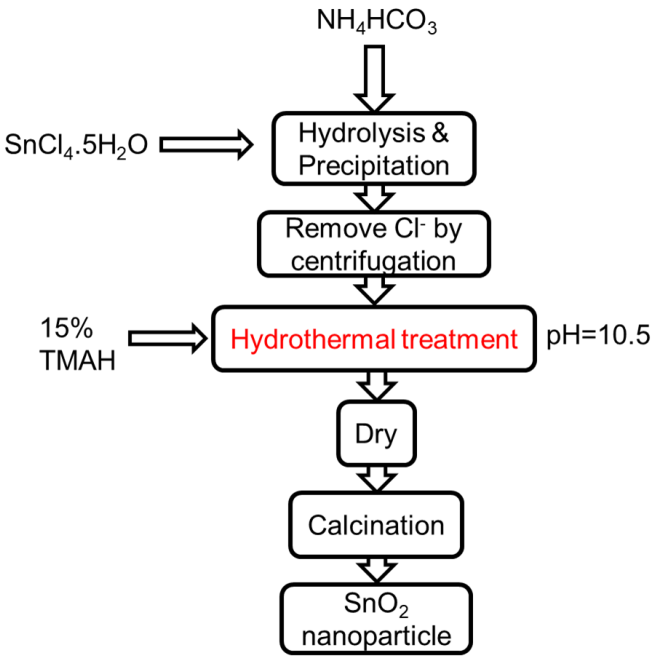

Fig. 3.1 Flowchart of SnO_2 synthesis with hydrothermal treatment

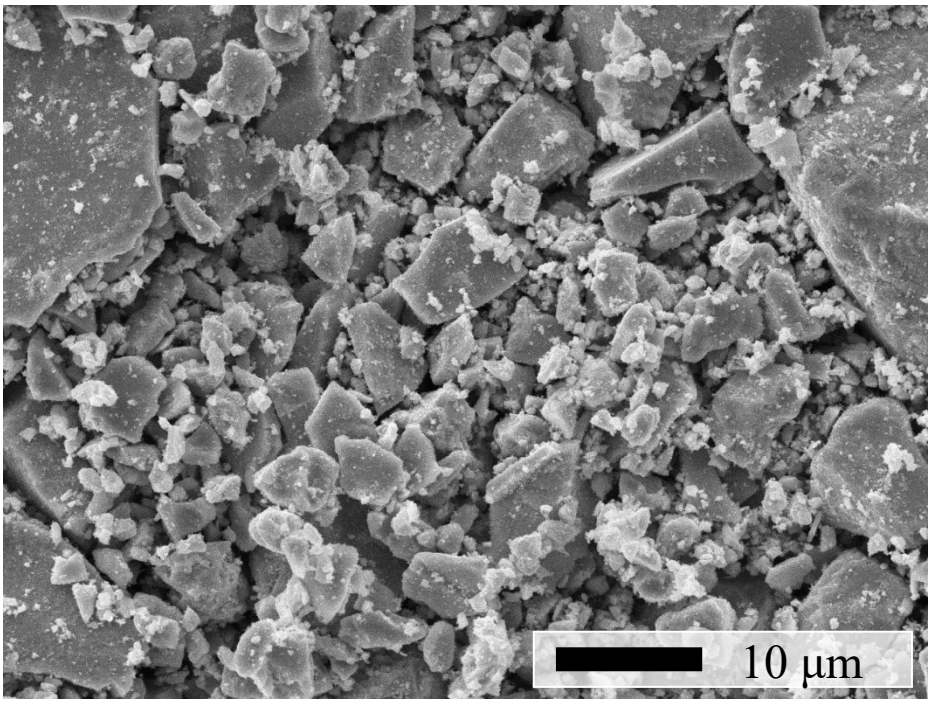

Fig. 3.2 SEM image of hydrothermally synthesized SnO_2

To investigate the secondary particle size effect on the gas sensor, a simple separation method is executed by sedimentation with water. The supernatant consists of fine secondary particles, while the precipitation consists of coarse secondary particles, as shown in Fig. 3.3. The fine secondary particles are constituted predominantly by 1 μm size. The coarse secondary particles are constituted predominantly by over 10 μm. The coarse SnO_2 is inappropriate for MEMS gas sensors because they have a secondary particle size larger than 50 μm. Therefore, the analysis of hydrothermally synthesized is operated on thick film gas sensors, when the effect of electrode size is minimized compared to MEMS gas sensors. Figure 3.4 displays the color of the sample we obtained, such as the yellowish-white sample is fine SnO_2, and the yellow sample is coarse SnO_2. The color might be caused mainly by secondary particle size. However, it arguably also be caused by different band configurations, with the coarse SnO_2 presenting more impurity levels in the band gap.

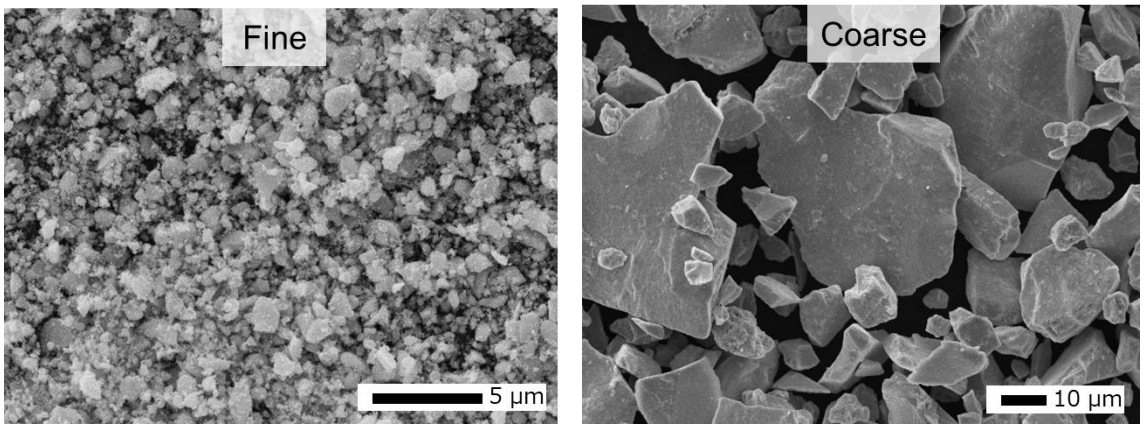

Fig. 3.3 Classification of hydrothermally synthesized SnO_2.

Fig. 3.4 Color of separated SnO_2 synthesized by hydrothermal treatment: white (left) is fine-SnO_2 and yellow (right) is coarse-SnO_2.

The fine SnO_2 can be implemented in thick-film and miniaturized gas sensors. However, the coarse SnO_2 is difficult to implement in both ordered sizes of gas sensors, needing to classify more. Nonetheless, the separation yield in a mass of fine SnO_2 is exceedingly low at 6.7% (for example, 67 mg of fine SnO_2 is obtained from 1g SnO_2), and it is inappropriate to proceed with gas-sensing and electrical measurement related to mass production and further investigation in receptor function properties by Pd loading. Despite low yield, the fine SnO_2 and coarse SnO_2 were implemented in a thick-film gas sensor, with the detailed results discussed in Chapter 4.1.

3.3 Characterization of classified SnO_2 – as-synthesized SnO_2

As cited in the previous subchapter, the agglomeration process arguably occurs in the drying process and potentially the nuclei or primary particles formed in the hydrothermal process promote the large particle formation. Therefore, the tin dioxide prepared without a hydrothermal process might have a little of coarse secondary particles. The synthesis method is mentioned in Chapter 2. Fig 3.5 shows the XRD results of fine and coarse SnO_2 and the reference pattern on ICSD (ICSD-92552[24]). The crystal structure is the rutile structure with $P4_2/mnm$ space group for both separated samples. The average crystallite size was almost the same with 16-17 nm, calculated with Scherrer's equation and mean of 110, 101, 211 facets. With these results, the primary particle size is conserved. The micro-size morphology is shown in Fig. 3.6. The tin dioxide without hydrothermal treatment showed predominantly a smooth shape and many fine secondary particles.

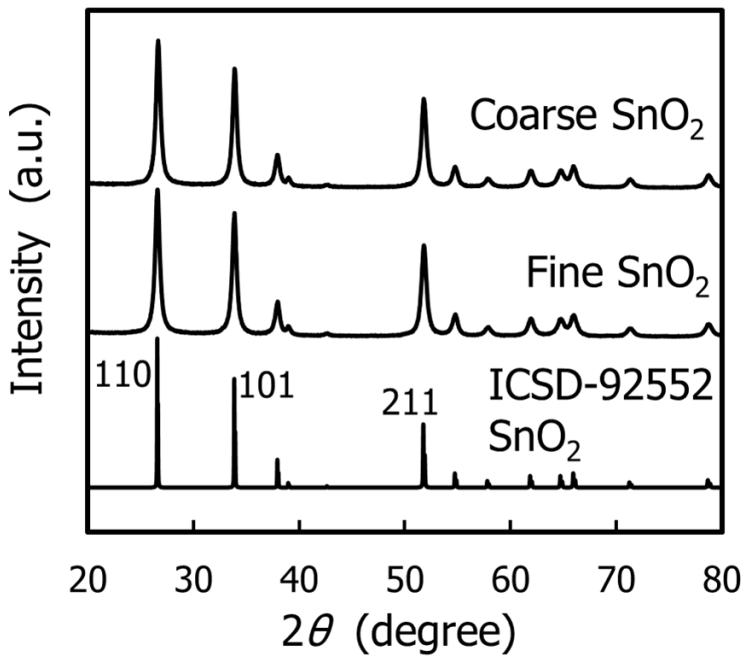

Fig. 3.5 XRD of fine and coarse SnO_2.

The separation process was proceeding successfully. Even though the fine and coarse SnO_2 are separated adequately, they seem to have no uniform secondary particle size. The grain size effect is deeply discussed by Yamazoe et al. [54, 82, 85], though is not related directly to the secondary size effect. Therefore, the sample adequate for secondary particle size investigation is a sample with a narrow particle size distribution, which avoids such a non-uniform micro size effect. Fig. 3.7 shows the color of separated SnO_2. The fine and coarse have a similar color, but the coarse is more dark yellow color. The tendency is the same with hydrothermally synthesized SnO_2, however, the coarse-SnO_2 is darker for it than without hydrothermal. These shows simply by the extremely larger particles are avoided in as-synthesized coarse SnO_2.

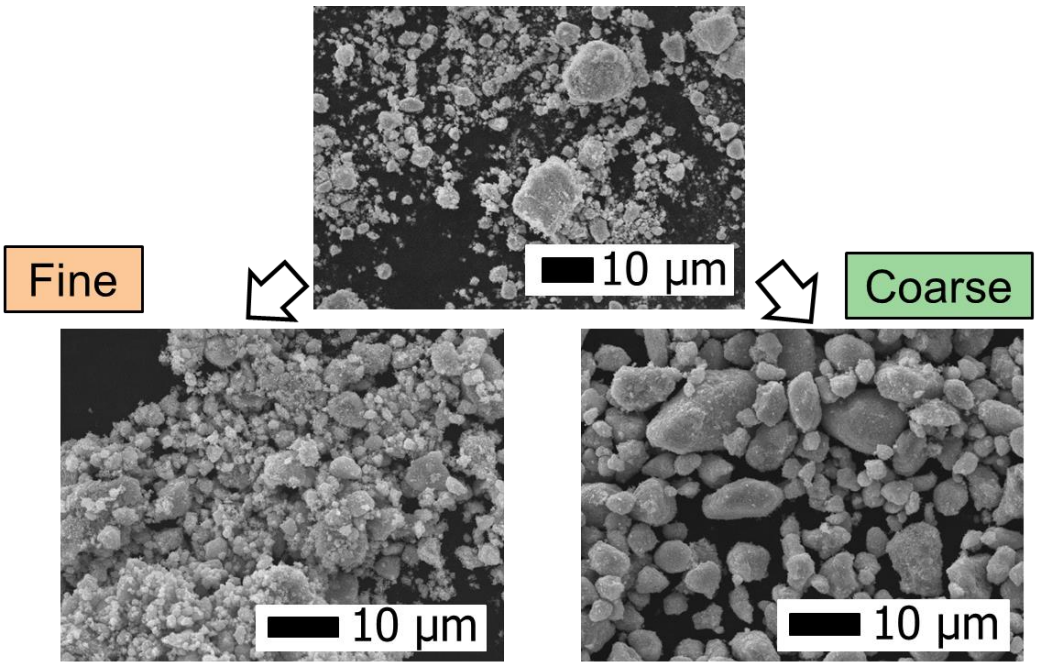

Fig. 3.6 SEM image of as-synthesized SnO_2 and separated samples

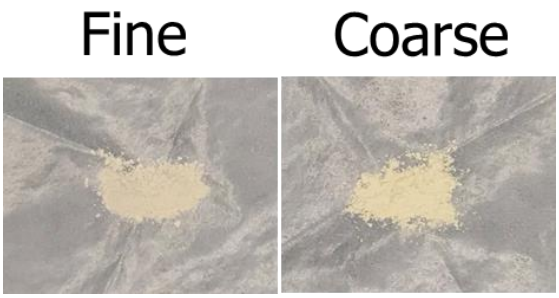

Fig. 3.7 Color of separated SnO_2; identical tendency with hydrothermal treatment.

Fig. 3.8 shows the particle size distribution of fine- and coarse-SnO_2 measured by laser scattering, in volume percentage. The coarse shows a relatively narrow distribution than fine-SnO_2. The fine shows a broader size distribution creating overlap with coarse particles. The volume percentage graph might cause these. The ratio of 1 μm and 10 μm particles in volume is 1000, which means that 1 coarse particle is equivalent numerically with 1000 fine particles. Therefore, even if the number of fines is high in the SEM image, the fine-SnO_2 showed a wider distribution. Analogically, the coarse SnO_2 presents higher fine particles in SEM images than in PSD. For detailed analysis, it is suggested that more classification processes for each fine and coarse. Nevertheless, the more classification will abruptly decrease the total yield of each separated sample. Therefore, it is better to modify the drying process to intrinsically make the narrow particle size distribution. Even with the potentially wider distribution, we made the sensor using these separated materials, principally because the median particle size is separated from 1 ordered size (fine: 2 μm, coarse: 20 μm). Such differences might cause drastic distinguished results in thick film and more in MEMS gas sensors.

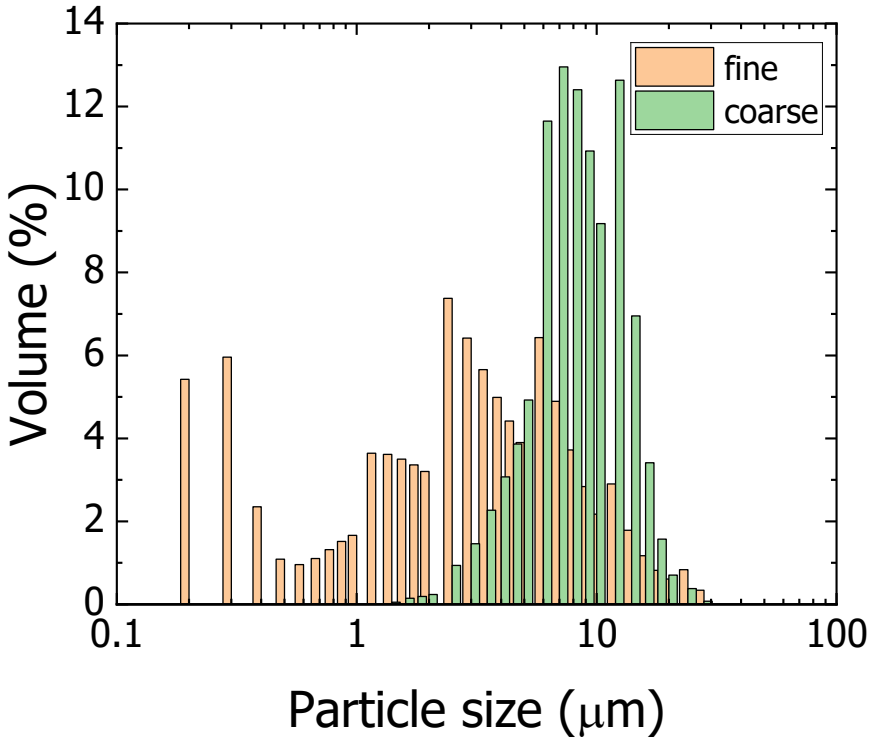

Fig. 3.8 Particle size distribution of fine and coarse SnO_2.

For the as-separated sample, the specific surface area, pore volume, and pore size distribution were calculated by the BET-BJH method from N_2 adsorption/desorption measurement. Fig. 3.9 shows the pore size distribution calculated by the BJH method of fine and coarse SnO_2. The pore size tendency below 10 nm is similar, representing a similar specific surface area calculated by the BET method. Since 20 nm, the fine SnO_2 shows a constant increase, but coarse SnO_2 shows a decay since 40 nm, resulting in a larger pore volume for fine SnO_2. The pore around 20-50 nm might void space formed by a cluster of primary particles (~100-200 nm). In fine SnO_2, the pore around 50-200 nm might void space formed by secondary particles (~ 1-2 μm). Hence, the coarse SnO_2 will have a pore formed by secondary particles (~ 20 μm) in 1000-2000 μm, nevertheless unmeasurable in N_2 adsorption/desorption measurement.

The mesoporous range (2-50 nm) is considered the Knudsen diffusion dominance, the effective way for gas reaction and diffusion. Interestingly, the mesoporosity of fine and coarse is identical, however until 200 nm the fine shows a high value, where the Knudsen diffusion might still be dominant or considerable to gas diffusivity. It is valuable to note that the pore structure measured denotes the intrinsic properties, not directly applicable for gas sensor material properly because the presence of organic impurities comes from the solvent to perform the paste.

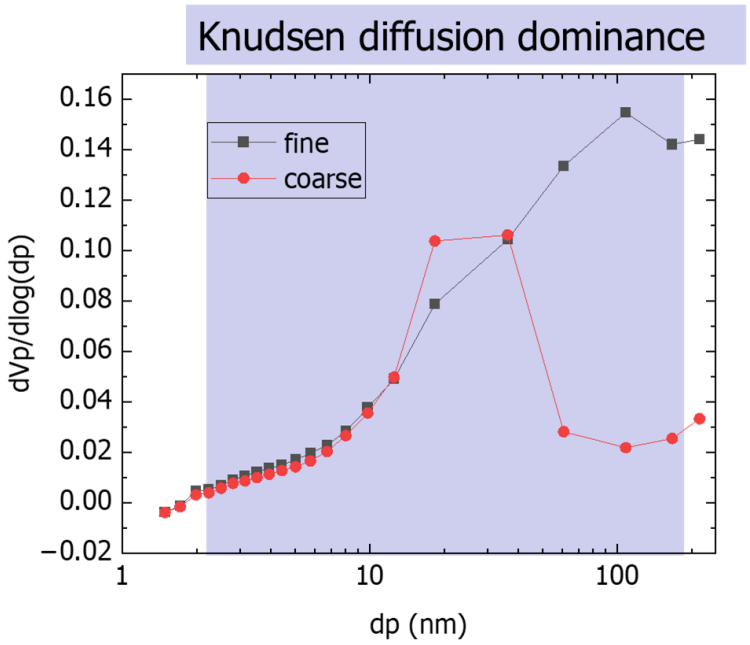

Fig. 3.9 BJH results of fine and coarse SnO_2.

Table 3.1 summarizes the BET/BJH results. The pore volume of fine is doubly higher than coarse SnO_2. The BET-specific surface area is almost equal. The average pore diameter is larger for fine samples, nonetheless, both have Knudsen diffusion.

Table 3.1 Pore volume and specific surface area of fine and coarse SnO_2.

	Fine	**Coarse**
Pore volume (cm^3g^{-1})	0.17	0.09
BET specific surface area (m^2g^{-1})	22.0	18.5
Average pore size (nm)	30	20

The tin dioxide synthesized without hydrothermal treatment showed an equilibrated separation mass yield, with 36% for fine and 42% for coarse. The obtained yield is more plausible for this research when the main topic is investigating the effect of secondary particle size (for example, approximately 0.4 g for each separated SnO_2 can obtained from 1 g of SnO_2). The hydrothermal treatment is important to obtain a geometrically stable sample. Nevertheless, the tin dioxide synthesized without hydrothermal treatment maintains a relatively mono-dispersed and close to the spherical shape of primary particles, even though the size of the crystal is larger for material without hydrothermal treatment (with Hydrothermal: 12 nm, without Hydrothermal: 16 nm).

3.4 Characterization of top-down technique to fine-SnO_2

Aware of the material non-compatibility with MEMS gas sensors, the top-down technique was performed to obtain a highly fine SnO_2 powder. Hypothetically, the dissolved Sn and OH ions are the main cause of larger agglomeration. Thus, there are two methods to overcome: freeze drying and solvent substitution [86]. This research was executed through solvent substitution by ethanol. Fig. 3.10 shows the flowchart of ethanol rinsed version of tin dioxide powder synthesis. After the chloride and ammonium ion removal process, the gel is rinsed with ethanol 2 times. Only 1 rinse cycle is not enough, creating a partial solvent state that keeps the same or creates a wider distribution. After 3 times rinse, the difference is small. Thus, 2 times ethanol rinse is elaborate to this synthesis method.

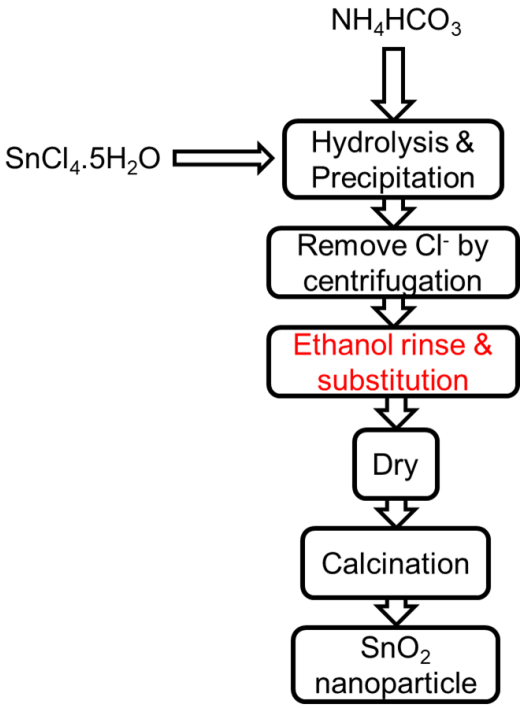

Fig. 3.10 Flowchart of ethanol rinsed SnO_2.

The micro-size morphology is shown in Fig. 3.11. The 10 μm order size disappeared in ethanol-rinsed SnO_2 powder. The prepared SnO_2 consists predominantly of particles with less than 1 μm. Hence, the particle distribution is non-uniform with 78% fine and 10% considered coarse. Moreover, the large particle with 5 μm is easily breakable with agate mortar. Therefore, this material is not appropriate for this research. Nonetheless, the material potentially is appropriate for MEMS gas sensors to achieve high reproducibility in terms of electrical resistance and gas-sensing behavior, besides the extremely low electrical resistance by negligible electrode-particle contact resistance.

MEMS gas sensors require a material and device manufacturing that provides high reproducibility and low electrical resistance in the operating temperature range (200-400ºC). Conventional material has irregularly larger particles, particularly over 10 μm, that cause high electrical resistance compared to another sensitive membrane that does not: this is the origin of low reproducibility. The ethanol-rinsed SnO_2 could overcome the reproducibility issue. However, the extremely fine SnO_2 makes the sensitive membrane dense, inhibiting molecular diffusion. In some cases, it is possible to adjust the thickness of sensitive membranes to solve this issue but limited to not extremely large gas molecules.

The classification of ethanol-rinsed SnO_2 is shown in Fig. 3.12. The fine is less than 1 um and the coarse is around 2 μm. Therefore, for MEMS application, both seem a plausible material, even though the coarse has a 10% yield, while the fine has 78%.

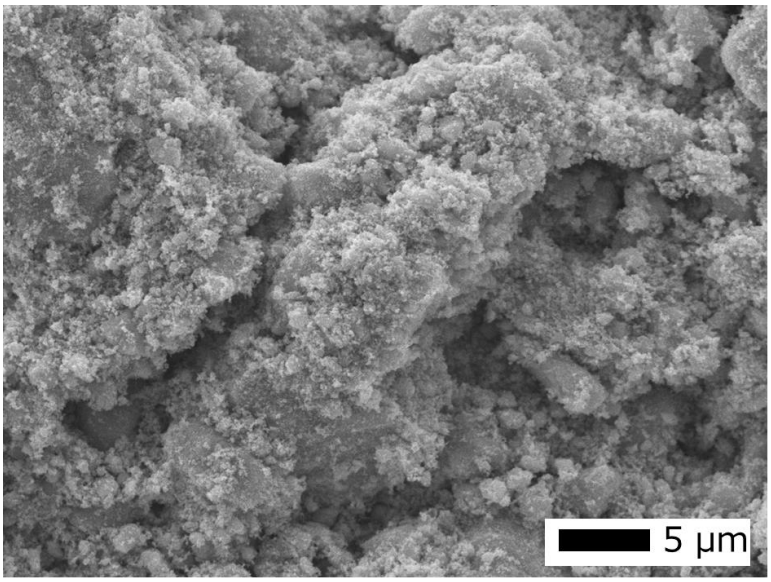

Fig. 3.11 SEM image of ethanol-rinsed SnO_2.

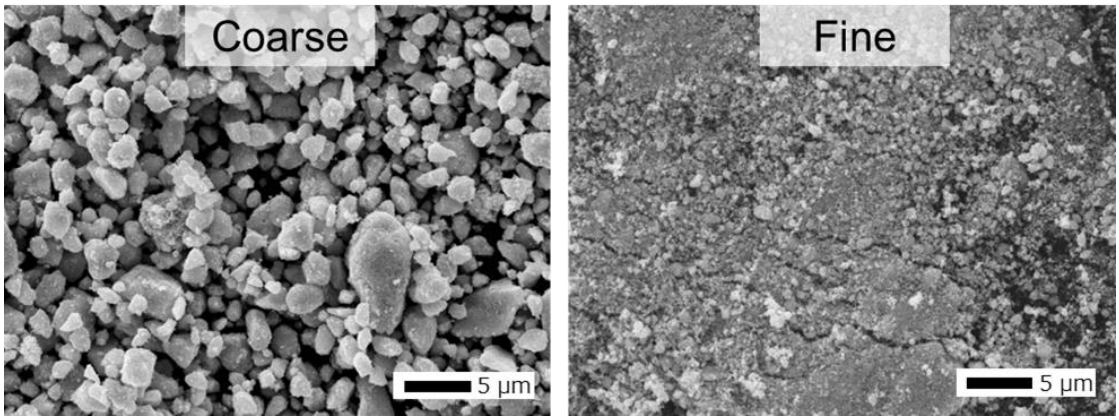

Fig. 3.12 SEM image of fine and coarse ethanol-rinsed SnO_2.

Even though the material is elevated to 600ºC for calcination, the as-synthesized and ethanol-rinsed SnO_2 have different pore properties by the BET method. Fig. 3.13 shows the BJH pore distribution results of fine and coarse SnO_2 and Table 3.2 summarizes the pore properties of ethanol rinsed SnO_2. The average pore diameter is augmented 2 times, creating a peak shift to the right (high pore size) in pore size distribution. However, is not just a shift, but has an increasing of maximum dVp/dlog(dp), mainly at 40-50 nm. This was caused mainly by fine secondary particles. Although the BET-specific surface area exhibits a slight increase in the ethanol-rinsed sample, there is an increase in several independent primary particles in addition to the pores formed by clusters of primary particles. In other words, the ethanol-rinsing approach could avoid the formation of secondary particles.

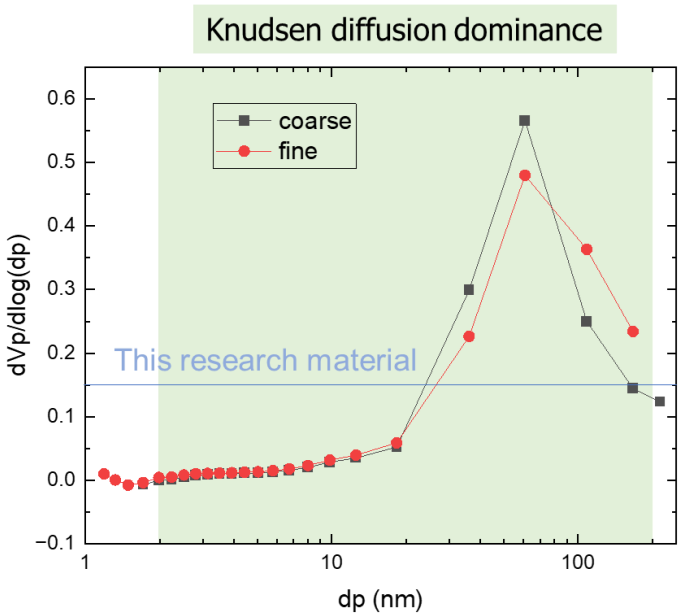

Fig. 3.13 BJH results of ethanol rinsed SnO_2.

Table 3.2 Pore properties of ethanol-rinsed SnO_2 and as-synthesized SnO_2.

	Ethanol rinsed SnO_2		**As-synthesized SnO_2**	
Pore properties	**Fine**	**Coarse**	**Fine**	**Coarse**
Pore volume (cm^3g^{-1})	0.32	0.32	0.17	0.09
BET specific surface area (m^2g^{-1})	29.0	29.5	22.0	18.5
Average pore size (nm)	42	43	30	20

3.5 Summary

This chapter showed the hydrothermal treatment, without hydrothermal treatment and ethanol-rinsed SnO_2 synthesis characterization results, focused on XRD, SEM, PSD, and BET-BJH.

The following summarizes the knowledge acquired:

(1) Hydrothermal synthesis of SnO_2 has a lot of coarse and ethanol rinsed SnO_2 has a lot of fine SnO_2. Both are not appropriate for this research.

(2) Without hydrothermal synthesis (as-synthesis method) SnO_2 has a uniform particle size distribution. This material is appropriate for this research.

(3) Ethanol rinsed SnO_2 is a peculiar material with tremendously fine secondary particles that cause an exceedingly high pore property with double average pore size and volume. This adequate use of this material could be more appropriate for MEMS gas sensors.

4. Electrical and gas-sensing properties of secondary particle size-varied tin dioxide

4.1 Introduction

4.2 Electrical and gas-sensing properties of hydrothermally synthesized SnO_2 on thick-film gas sensors with different secondary particle size

4.3 Electrical and gas-sensing properties of as-synthesized SnO_2 on miniaturized gas sensors with different secondary particle size

4.4 Electrical and gas-sensing properties of as-synthesized Pd-SnO_2 on miniaturized gas sensors with different secondary particle sizes

4.5 CO-catalytical combustion and TPR measurements

4.6 Summary

4.1 Introduction

The previous chapter established the classification method with no hydrothermal treatment SnO_2, as mentioned and explained in Chapter 2. Now, the sensor device is made and measured using this separated material. Meanwhile, the hydrothermally synthesized SnO_2 gas sensor is also analyzed, especially in thick film sensors where the resistance effect of particle-electrode contact is minimized compared to MEMS gas sensors. Afterward, the receptor function (one of the three principal key factors in sensor design) is verified for different secondary particle sizes, if they have peculiar behavior. Finally, to compare differences in chemical properties for gas sensors, the CO catalytical combustion and temperature-programmed reaction are evaluated on fine and coarse SnO_2 and Pd-loaded samples.

The main electrical property of SnO_2 gas sensors is electrical resistance. As detailed in Chapter 1, SnO_2 is a semiconductor material that varies the surface charge density with adsorbate interaction, such as chemisorption or ionosorption. The electrometer can measure this variance in electrical resistance, ranging from 10^3 to 10^{10} Ω. For a thick film sensor, the maximum measurable resistance is 10^8 Ω, which is limited by the alumina substrate of the sensor device. After the 10^8, the signal-to-noise ratio is decreased, making it difficult to distinguish signal from noise. The same occurs with the MEMS gas sensor, however at 10^6 Ω. Therefore, in terms of detection and low cost of the data acquisition system, the sensor with low electrical resistance and high sensor performance is ideal.

The gas-sensing properties are focused on sensor response, represented by the ratio between electrical resistance in air and target gas. The reaction is continuous and depending on gas molecular, concentration, and temperature, the electrical resistance is late to achieve an equilibrium. Measuring the electrical resistance while waiting for the equilibrium state is ideal for achieving precision and accuracy. Nevertheless, depending on the gas reduction property of SnO_2, long-time exposure to gas damages the SnO_2 surface (deactivation or deterioration). Thus, the effective way to measure the sensor response is by sampling the electrical resistance immediately before the equilibrium. In this research, continuous sampling is executed.

The problem of deterioration will occur in CO catalytical combustion, mainly at

low temperatures. CO gas has a peculiar reduction property against the SnO_2 surface, eventually observing the catalytical deactivation at low temperatures with mass number *m/z* 28 for CO and *m/z* 44 for CO_2. Meanwhile, the temperature-programmed reaction during rinsing temperature shows a desorption gas composition in MS, subsequently, it can be estimated the adsorption properties of CO on SnO_2 that might be related to gas-sensing properties.

4.2 Electrical and gas-sensing properties of hydrothermally synthesized SnO_2 on thick-film gas sensors with different secondary particle size

The thick-film gas sensors are made by screen-printing, preparing the paste with the α-terpineol ($C_{10}H_{18}O$, 98% purity, Fujifilm Wako Pure Chemical Corporation). The powder-solvent ratio controls the paste viscosity and thus is dependent on sample affinity to α-terpineol. The prepared thick film is dried and calcined at 550ºC. Fig. 4.1 shows the SEM image of the cross-sectional view of fine and coarse SnO_2 on the thick-film sensor, constituted by alumina substrate and interdigitated Au-electrode. The sample is fixed into resin and cut with a diamond cutting machine. The coarse and fine secondary particles' size and shape remained the same immediately before the sensor preparation SEM image. Supposedly, the coarse SnO_2 gas sensor shows a lot of macropores in tens micron size and the fine SnO_2 gas sensor is more compact yet with macropores in sub-micron size.

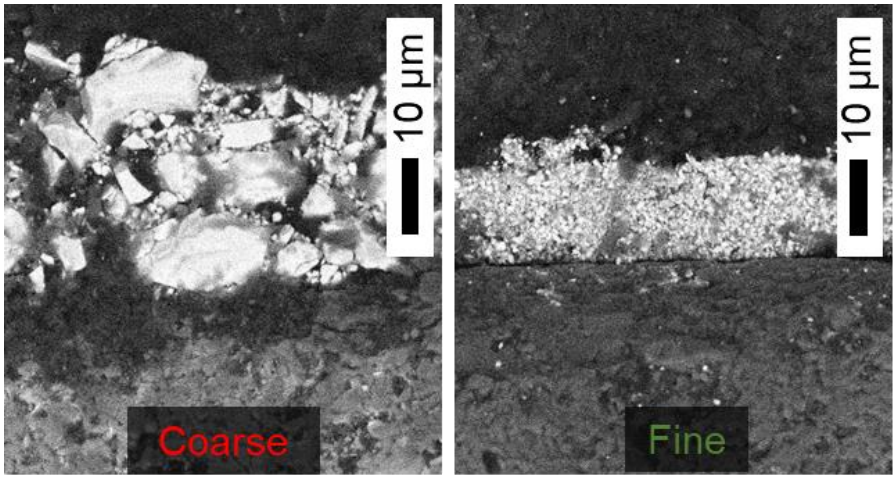

Fig. 4.1 Cross-sectional view of fine and coarse SnO_2 (white material) on alumina substrate (bottom material).

The prepared thick film sensor is positioned in a gas measuring system. Fig. 4.2 shows the electrical resistance measured for H_2 and CO gas. As mentioned, these gases are simple gases to learn a fundamental property of new material. The coarse SnO_2 shows mostly a higher electrical resistance than fine SnO_2. Furthermore, the fine SnO_2 also presented higher decay when the H_2 and CO gas were flown on the system (green arrows) than coarse SnO_2 signal variation (red arrows). The simple gases' behavior is similar. Hence, it is worthy of a numerical transformation of the curves. The popular analysis between electrical resistance and temperature is the Arrhenius plot. Arrhenius plot is a graph plotted with the reciprocal of the absolute temperature (in kelvin) on the x-axis and the natural logarithm of the reaction rate constant on the y-axis. The electrical resistance of the gas sensor is hypothetically related to the gas reaction; thus, this relation is valid even for electrical resistance. Fig. 4.3 shows the Arrhenius plot of fine and coarse SnO_2 in air and 20ppm H_2 and CO. They present a few linearities, more precisely, appears that the rate-limiting reaction/factor is different depending on temperature. The measurement required is a short-range operating temperature operated in low and high temperatures separately. Although the plot does not appear linear, the coefficient of determination was higher than 0.9, thus, allowing more detailed analysis on them.

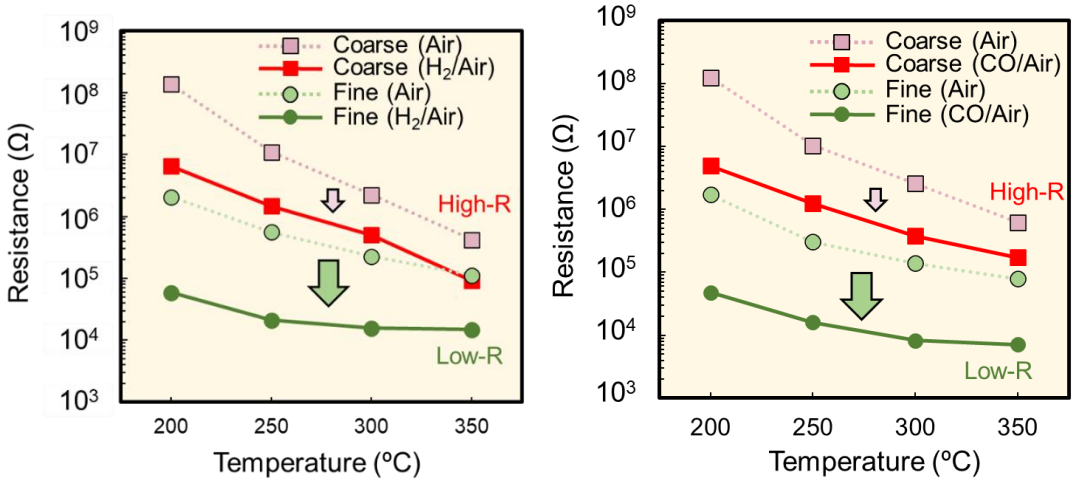

Fig. 4.2 Electrical resistance of fine and coarse SnO_2 in air and 20 ppm H_2 and CO

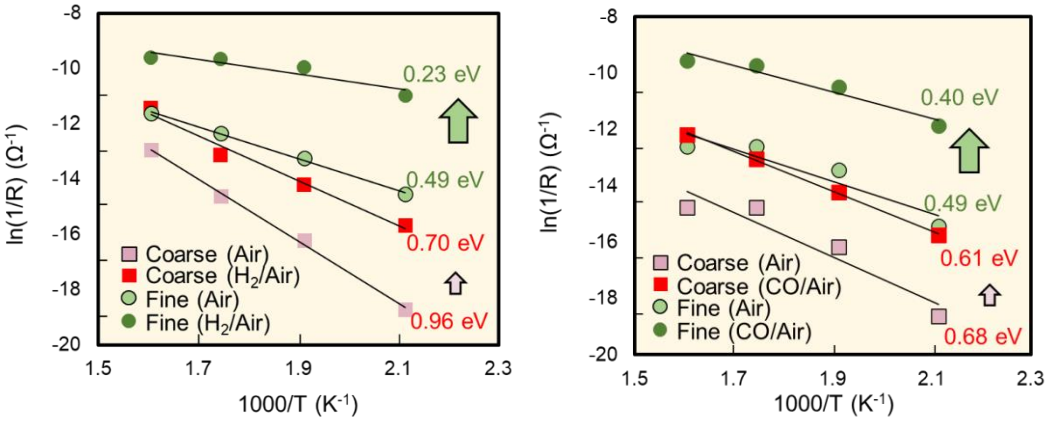

Fig. 4.3 Arrhenius plot of electrical resistance in air of fine and coarse SnO_2

Tables 4.1 and 4.2 show the activation energy calculated from the Arrhenius plot via slop extracting for linear regression. Δ is the activation energy variation in air and target gas. The activation energy of coarse SnO_2 in air varies between H_2 and CO. The sensitive membrane of coarse SnO_2 is rough and fragile. These differences are attributed to the instability measurement. In air, the activation energy of coarse is higher than fine SnO_2. This means that the coarse SnO_2 requires more energy for the surface reaction or the reaction-resistance transformation. Focused on the same material, the activation energy in this case means the reaction-resistance transformation, in other words, how many resistive components that participate in surface charge reaction are in the gas sensor. Coincidentally, the variation of activation energy between air and H_2 and between air and CO were equal, representing that the effective resistive component is the same in coarse and fine SnO_2.

Table 4.1 Activation energy of fine and coarse in air and H_2

Activation energy (eV)	Air	H_2	Δ
Coarse	0.96	0.70	0.26
Fine	0.49	0.23	0.26

Table 4.2 Activation energy of fine and coarse in air and CO

Activation energy (eV)	Air	CO	Δ
Coarse	0.68	0.61	0.07
Fine	0.49	0.23	0.09

The resistive component on gas sensors is grouped by (R_1) bulk resistance, (R_2) inter-particle resistance, (R_3) inter-secondary particle resistance, and (R_4) electrode-particle resistance, illustrated in Fig. 4.4. The number of R_1 and R_2 is proportional to the density of sensitive membrane, so are similar in fine and coarse. On the other hand, the number of R_3 and R_4 is exceedingly lower for coarse SnO_2 (summarized in Table 4.3). The low number of R_3 and R_4 provides a limited electron path of coarse SnO_2 that causes high electrical resistance points. Another discussion about the high electrical resistance cause is the conductivity variated by percolation between secondary particle and void proportion. The percolation theory is mostly used for filler particle conductivity analysis but is applicable for sensitive membranes. When the particle concentration on the sensitive membrane is higher than the percolation threshold, the electron path is defined. If is lower than the percolation threshold, the electron path is not defined. The fine should be higher than the threshold, however the coarse is in percolation transition, when the electron path is limitingly established, having the electric conductivity between dielectric and metal (oxide). Therefore, the fundamental electrical resistance of coarse SnO_2 is higher than fine SnO_2 (R_3, R_4), meanwhile, the sensitive electrical resistance is equal for both (R_1, R_2). The sensor response is defined by the ratio between electrical resistance in air and in target gas. Therefore, the total variance of the sensitive electrical resistance is low to coarse SnO_2, resulting in a low sensor response (summarized in Table 4.4).

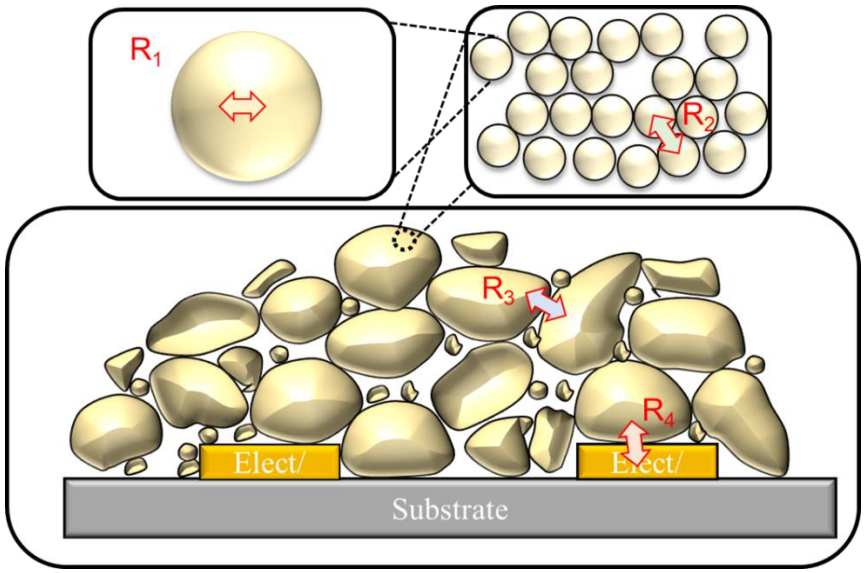

Fig. 4.4 Model of gas sensor and resistive components.

Table 4.3 Resistive component on the gas sensor and number of contacts.

	Resistive component	Total number
R_1	Bulk resistance	Coarse ≈ Fine
R_2	Inter-primary particle resistance	Coarse ≈ Fine
R_3	Inter-secondary particle resistance	Coarse < Fine
R_4	Electrode-particle resistance	Coarse < Fine

Table 4.4 Speculation of sensitive resistive components.

	R_{3air}, R_{4air}	R_{1air}/R_{total_air}, R_{2air}/R_{total_air}	R_{total_air}	S
Coarse	High	Low	High	Low
Fine	Low	High	Low	High

Even though was possible to identify speculation against the responsible resistive component to sensor response, distinguishing R_1 to R_2 was not possible. For further analysis, the use of electrochemical impedance spectroscopy is required. Moreover, adjusting the electrode distance helps the identification of inter-secondary particle R_3 against R_4.

4.3 Electrical and gas-sensing properties of as-synthesized SnO_2 on miniaturized gas sensors with different secondary particle size

The electrical influence was discussed in subchapter 4.2, especially for thick film gas sensors. Now miniaturized gas sensors use SnO_2 as mentioned in the previous chapter, the SnO_2 with uniform particle size distribution. The difference between those used in the previous subchapter is that the coarse SnO_2 does not have extremely large particles yet 20-micron of median size. Fig. 4.5 shows the profile of fine and coarse SnO_2 on MEMS gas sensors. The fine has a dome-ish profile, while the coarse has a truncate cone profile. The profile and thickness are important to the gas diffusion mechanism and temperature-storing capability. The thickness is approximately 20 μm for both. The truncate profile is caused by affinity with glycerol, or the 20-micron median size is not appropriate to make a dome-ish profile gas sensor. Nonetheless, this result needs to be considered for sensor

response.

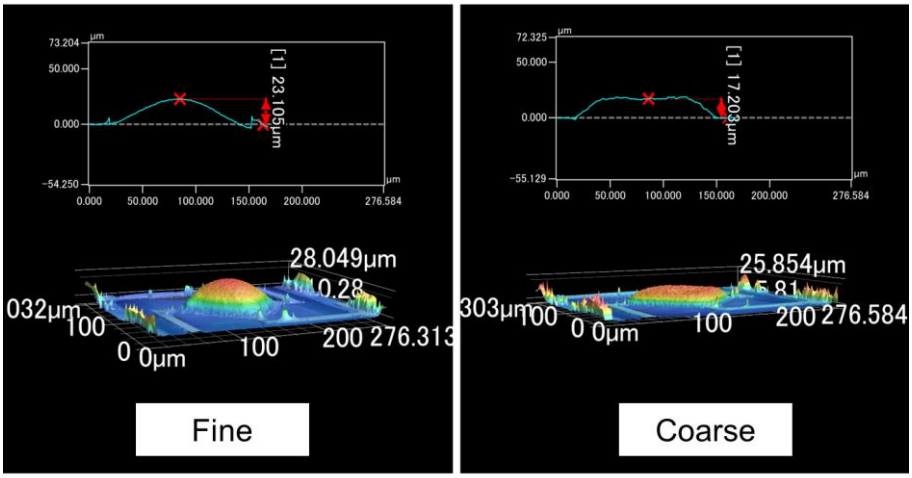

Fig. 4.5 Profile of MEMS gas sensor of fine and coarse SnO_2

Fig. 4.6 shows the electrical resistance of fine and coarse SnO_2 in air. Compared to the previous subchapter results, the coarse has a slight resistance variance in temperature. The same occurs in fine, however has a reversal behavior in temperature below 300ºC, decreasing the resistance. The MEMS gas sensor is 10^6 times smaller than the thick film gas sensor. Therefore, miniaturized gas sensors are more sensitive to water gas contained in the cylinder, the system, and the material, which is accentuated at low temperatures. The graph shows two signals for each configuration to visualize the electrical resistance reproducibility between two sensors.

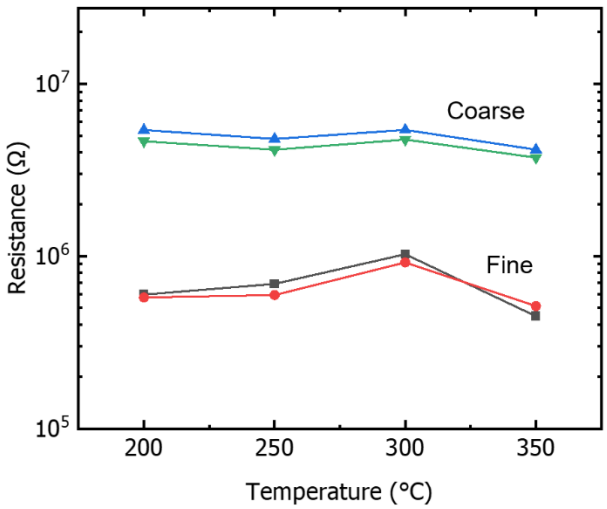

Fig. 4.6 Electrical resistance of fine and coarse SnO_2 in air

The electron conduction path model can also explain the electrical resistance differences between fine and coarse (Fig. 4.7). The high number of contacts promotes more electron path, and low electrical resistance. In contrast, the number of contacts is countable for coarse SnO_2 that promotes less electron conduction path - high electrical resistance. Particularly for fine SnO_2, the electron path is limited to the path near the electrode region, which limits the effective sensitive area close to the electrode.

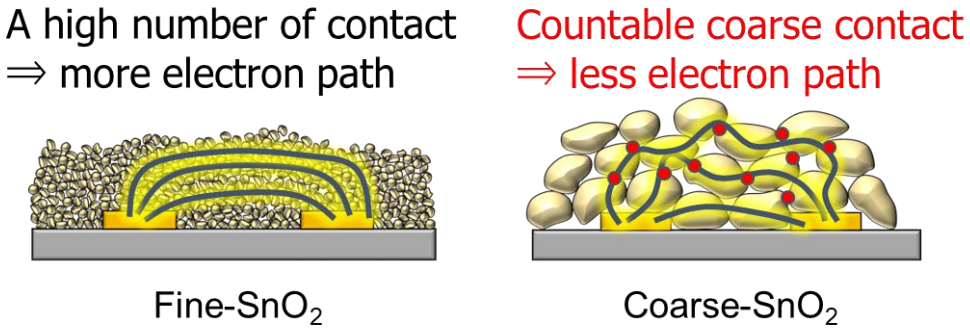

Fig. 4.7 Conduction path model for fine and coarse SnO_2 gas sensor

The gas concentration dependence on electrical resistance needs to have a linear relationship in a log-log plot, concerning the power law of the gas sensor [53], as in equation (1.3). The reducing gas often has a power of around -0.5. Consider 300ºC for the following analysis. Fig. 4.8 shows the electrical resistance and gas concentration dependence in H_2, CO, and C_2H_5OH at 300ºC. For hydrogen gas, the power was approximated to -0.5 for fine and coarse SnO_2.

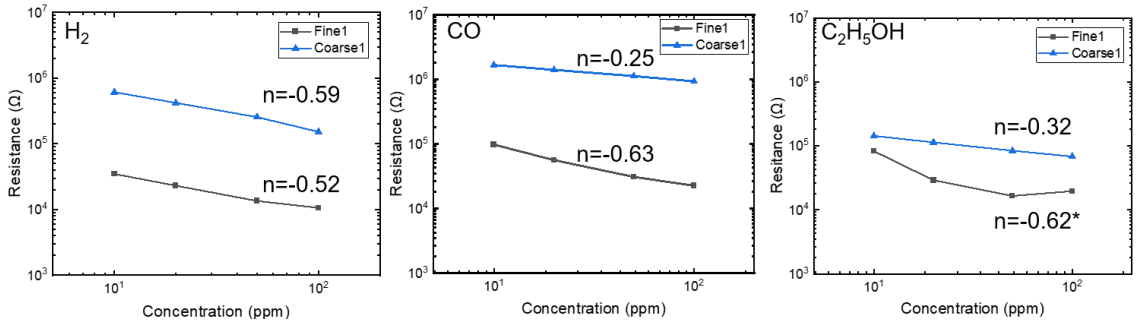

Fig. 4.8 Gas concentration dependence of miniaturized gas sensor in H_2, CO, and ethanol at 300ºC

However, with CO and C_2H_5OH gas showed different slope values. In CO gas, the fine SnO_2 presents a power value near -0.5, however, the coarse increased to -0.25, which means that the coarse has another reverse reaction that impedes the theoretical oxygen adsorption/desorption model of the metal oxide semiconductor gas-sensing mechanism. That occurs also in ethanol. Nevertheless, particularly for fine SnO_2, the graph does not show linearity, which means a dominant reverse reaction or another irrelevant factor caused this behavior. Fig. 4.9 shows the electrical resistance of fine and coarse SnO_2 in ethanol flow at 300ºC in time-dependence. The right graph shows the variation in the linear vertical axis. Since 10 ppm C_2H_5OH, the coarse SnO_2 showed transient behavior for all concentrations, meaning some deactivation or deterioration of SnO_2. The same occurs in fine SnO_2, but accentuated since 50 ppm, occurring reversal in 100 ppm with higher electrical resistance than 50 ppm. This is supposed that in fine SnO_2 is more susceptible to deactivation by CO reduction, however, the sensitive membrane is dense enough to not reach all gas close to electrodes. From 50 ppm, the considerable CO reaches the material near the electrode, actuating a deterioration more abruptly than coarse.

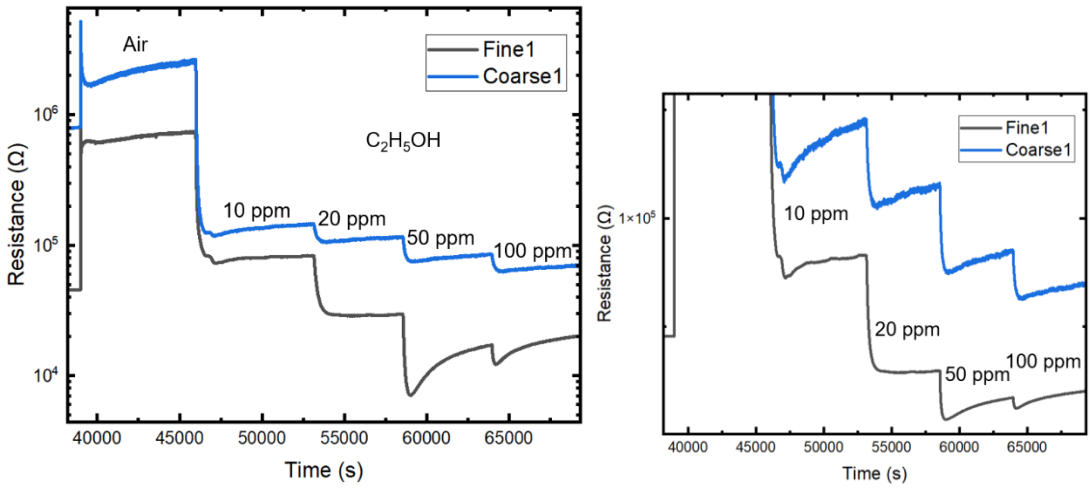

Fig. 4.9 Electrical resistance of fine and coarse SnO_2 in ethanol – time dependence, and the linear vertical axis (right)

Table 4.5 summarizes the relative standard deviation of 2 similar sensors for each separated sample. The RSD percentage value was less than 10% for both, representing numerically the high electrical reproducibility of the gas sensor for separated samples. Fig 4.10 illustrates the sensor response of fine and coarse in 100 ppm H_2, CO, and C_2H_5OH at 300ºC. Two gas-sensing behaviors occur regarding gas diffusivity: (1) Molecular diffusion in terms of gas molecular size, and (2) Knudsen diffusion in terms of effective particles participating in the gas-sensing.

Table 4.5 Relative standard deviation of fine and coarse between 2 similar sensors

	Fine	Coarse
Resistance (Ω)	9.7×10^5	5.0×10^6
RSD (%)	7.7	9

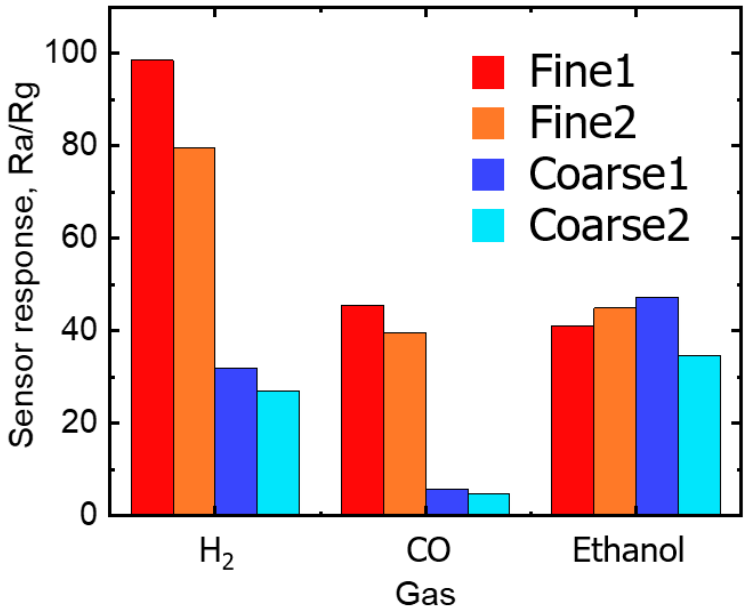

Fig. 4.10 Sensor response in 100 ppm H_2, CO, and ethanol at 300ºC

(1) Molecular diffusion (gas molecular size)

As mentioned, the sensitive membrane of the fine SnO_2 is dense and difficult for large gas diffusion such as ethanol (0.44 nm) [87]. Ethanol has twice to four times as CO and H_2 gas. Therefore, ethanol cannot diffuse into the region near the electrode resulting in a

lower sensor response than H_2 and CO, as shown in Fig. 4.11. As detailed in Chapter 1, SnO_2 is a mesoporous material where Knudsen diffusion acts throughout, responsible for gas sensing beyond the transducer function influenced by grain size control. Near the electrode, the Knudsen diffusion occurs more for coarse SnO_2 in ethanol gas, relating to a relatively higher sensor response.

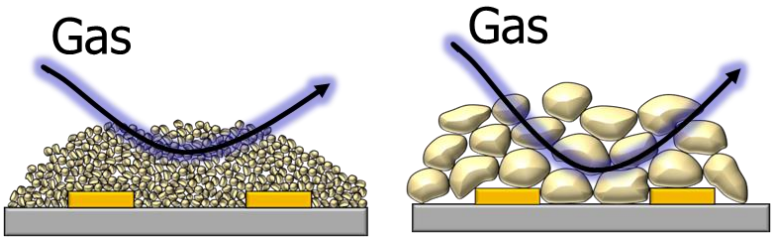

Fig. 4.11 Molecular diffusion into fine and coarse SnO_2 gas sensors

(2) Knudsen diffusion (secondary particle size)

In H_2 and CO, the filtering by gas molecular size does not occur. Almost all gas concentrations diffuse into the sensitive membrane. The Knudsen diffusion, a responsible diffusion for gas-sensing, occurs for entire fine secondary particle size and partially for coarse secondary particles. The gas concentration gradually decreases with the diffusion length. The primary particles near the surface of the secondary particle were entirely affected gas by Knudsen diffusion. On the other hand, the gas concentration at the center of the secondary particle is abruptly lower than that at the surface. This suggests that the fine particles of SnO_2 exhibit a more efficient use of Knudsen diffusion as a gas-sensing mechanism.

The previous subchapter discussed that the inter-primary particle is a resistive component responsible for gas-sensing. However, the inter-secondary particle becomes an important resistive component sensitive to gas reactions. Mainly for coarse SnO_2, the secondary particle electric variation summarizes the peculiar Knudsen diffusion effect on all primary particles. Thus, distinguishing the resistive component of SnO_2 on gas-sensing is crucial to determining the entire gas-sensing mechanism.

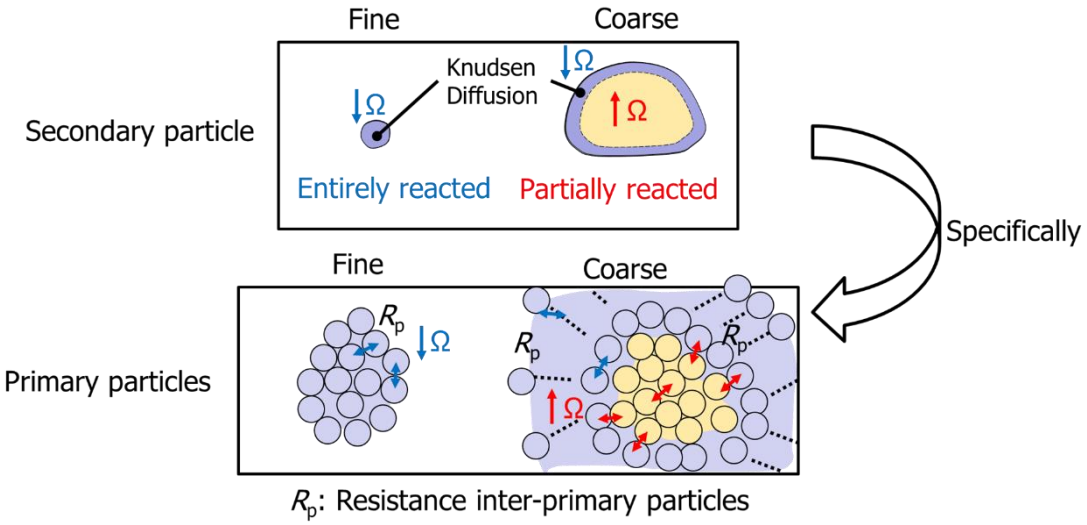

Fig. 4.12 Knudsen diffusion into fine and coarse SnO_2 gas sensors

4.4 Electrical and gas-sensing properties of as-synthesized Pd-SnO_2 on miniaturized gas sensors with different secondary particle sizes

Besides the secondary particle size effect on gas-sensing, the Pd-loaded SnO_2 evaluation for gas-sensing is crucial to high-performance gas sensor design. The Pd on SnO_2 has electronic and chemical sensitization effects as mentioned in Chapter 1. This subchapter will investigate the impact of secondary particle size on electronic and chemical sensitization effects. Fig. 4.13 displays the SEM image of fine and coarse SnO_2 after Pd-loading by impregnation method. The fine and coarse keep their respective size.

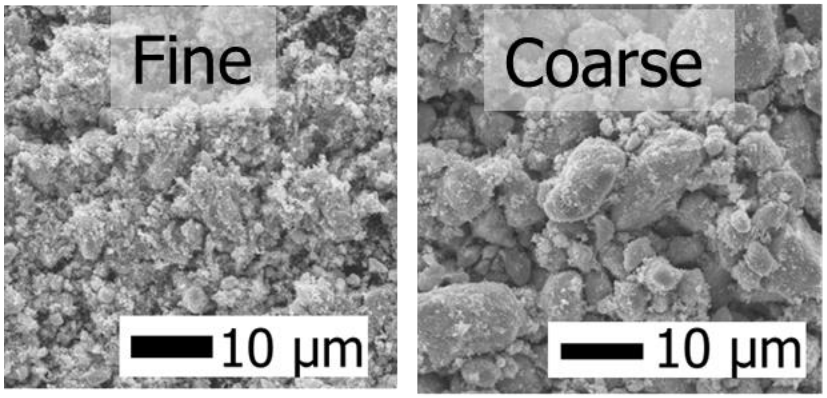

Fig. 4.13 SEM image of classified Pd-SnO_2

The electrical resistance in air was measured to Pd-loaded fine SnO_2 and coarse SnO_2, as shown in Fig. 4.14. Compared to the non-loaded sample, the electrical resistance was high, exceeding the detection limit of the MEMS device. The Pd-loaded fine and coarse SnO_2 show similar behavior in temperature dependence. Thus, the Pd-loaded effect might be more dominant than the secondary particle size effect.

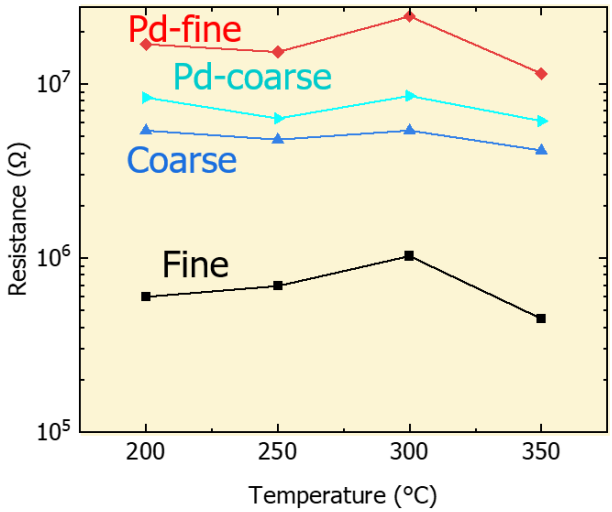

Fig. 4.14 Electrical resistance of fine and coarse Pd-SnO_2 in air

Fig. 4.15 shows the sensor response of Pd-loaded fine and coarse SnO_2 from 250ºC to 300ºC in 100 ppm ethanol flow. Pd-loaded fine SnO_2 showed predominantly higher sensor response than coarse, but also with the same behavior.

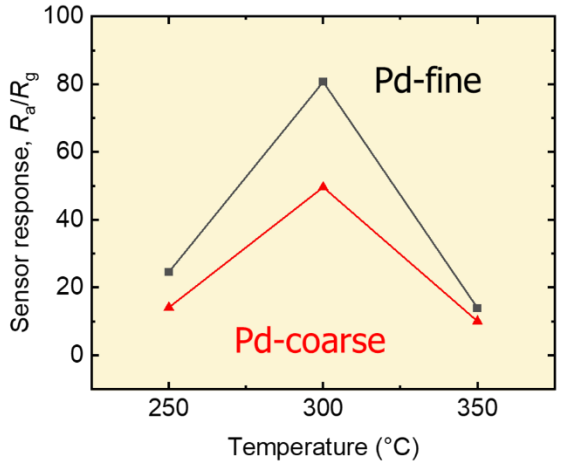

Fig. 4.15 Sensor response of fine and coarse Pd-SnO_2 in 100 ppm ethanol

The high electrical resistance of fine SnO_2 with Pd loading is attributed to the formation of an effective Pd particle cluster on the support. Electronic sensitization is associated with higher electrical resistance in the air. In the case of coarse SnO_2, the large Pd particle cluster was formed that hampered the electronic sensitization on SnO_2.

4.5 Catalytical combustion and TPR measurements

(1) Neat-SnO_2

There was a potential deactivation or deterioration of SnO_2 by CO combustion reaction, mainly at low temperatures. The combined gas chromatograph and mass spectrum analysis can explain these phenomena dynamically. Fig. 4.16 shows the catalytical evaluation of fine SnO_2 from 300 to 150ºC. At 350ºC, the CO_2 conversion rate slightly decreases yet almost 100%. At 100ºC, MS illustrates low *m/z* 44 evolution.

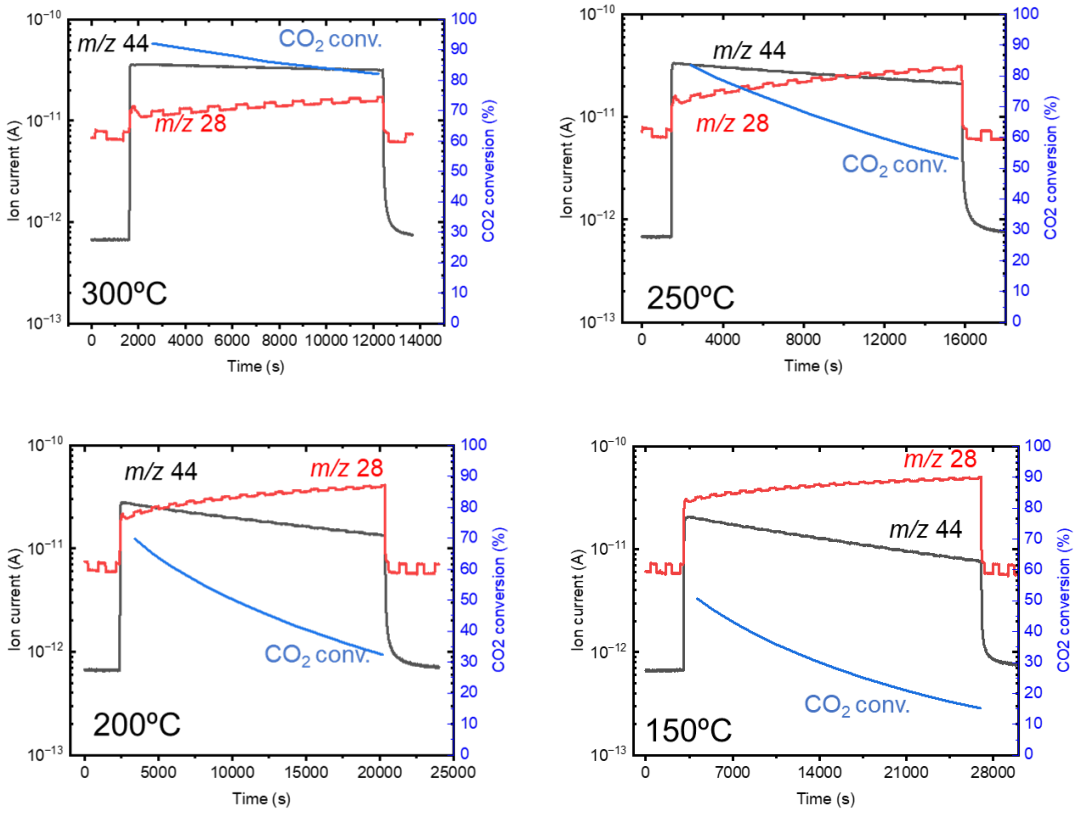

Fig. 4.16 Catalytical combustion of fine SnO_2 in CO gas flow.

The CO_2 conversion rate decreases during the catalytical combustion in agreement with *m/z* 28 which partially represents CO gas, the non-reacted gas portion. Therefore, CO deactivates the SnO_2 surface. The same phenomenon is observed in Fig. 4.17 for coarse SnO_2. It is worth noting that *m/z* 28 shows a rectangular shape. This might be caused by pressure loss that occurs in the four-way valve to shift to gas chromatography. The exhaust of gas chromatography is directly connected to the atmosphere; however, the exhaust of non-GC is connected to a trap with liquid paraffin. Fig. 4.18 shows the temperature dependence of fine and coarse SnO_2 of CO catalytical combustion, at the start and end of CO gas flowing. At 300ºC, the deterioration of SnO_2 by CO causes a decrease in CO_2 conversion rate. The decreasing rate in temperature dependence is equal for fine and coarse SnO_2, meanwhile, the fine SnO_2 is more susceptible a deactivation. This is because the fine SnO_2 has more adsorption points and effective diffusion into secondary particles.

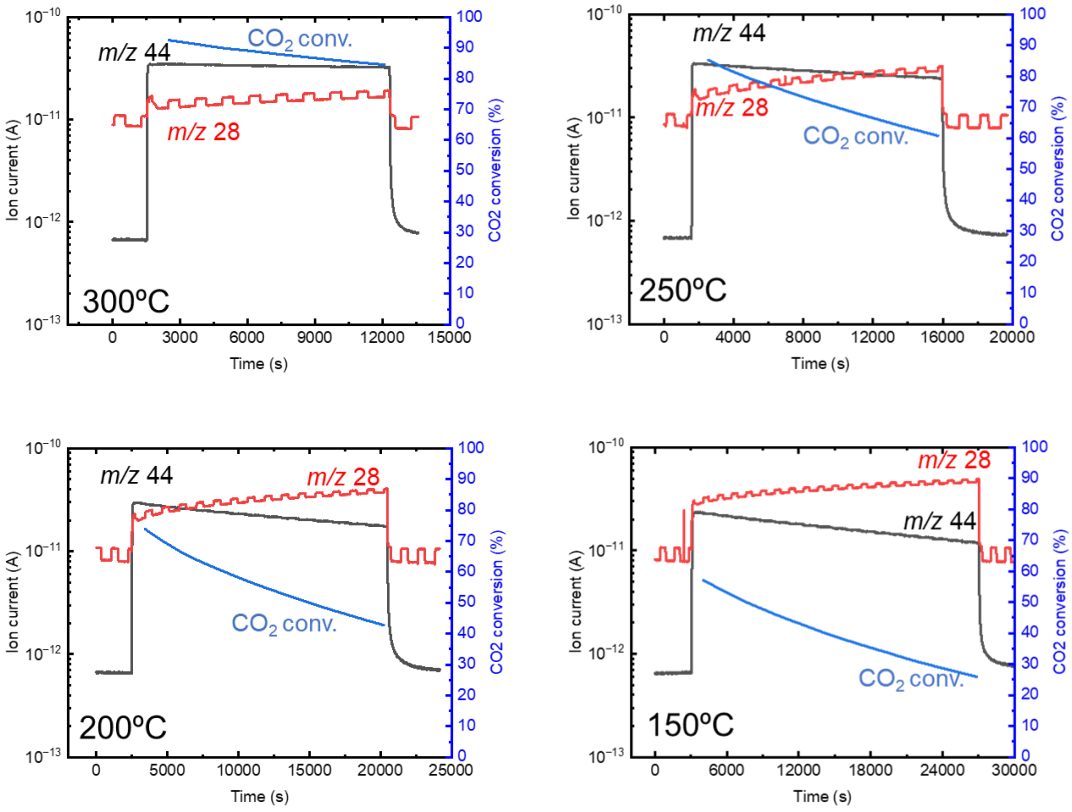

Fig. 4.17 Catalytical combustion of coarse SnO_2 in CO gas flow.

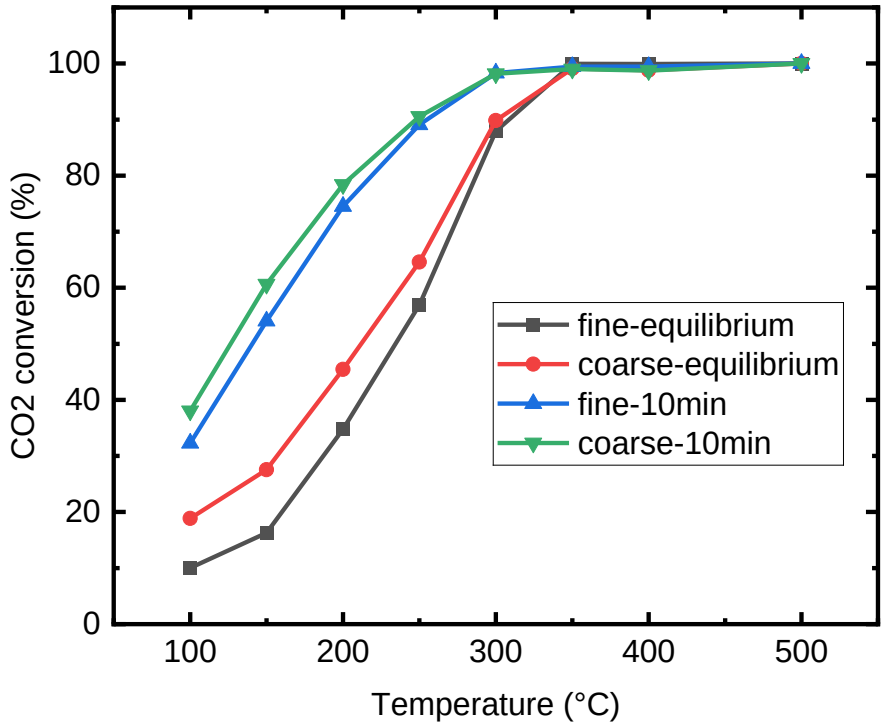

Fig. 4.18 Temperature dependence of fine and coarse in CO catalytical combustion.

The temperature-programmed reaction can be realized immediately after the CO catalytical combustion, raising the temperature to 550ºC. Fig. 4.19 and 4.20 show the CO-TPR measurement of fine and coarse SnO_2. As detailed before, the *m/z* 17 is to follow the H_2O or OH desorption due to the *m/z* 18 being influenced by Ar gas. The H_2O or OH desorbed is originated by material or system. The 150-550ºC CO-TPR for both separated materials showed three peaks in *m/z* 44 when the first (~220ºC) is physisorption of CO or CO2 on the SnO_2 surface (corresponding with behavior presented in Chapter 1) and the second and third peak (~275ºC, ~350ºC) are other forms of adsorption yet more strong. For investing this phenomenon, calcination in respective temperature and analyzing that in XPS to observe the nature of SnO_2 surface is the more versatile way.

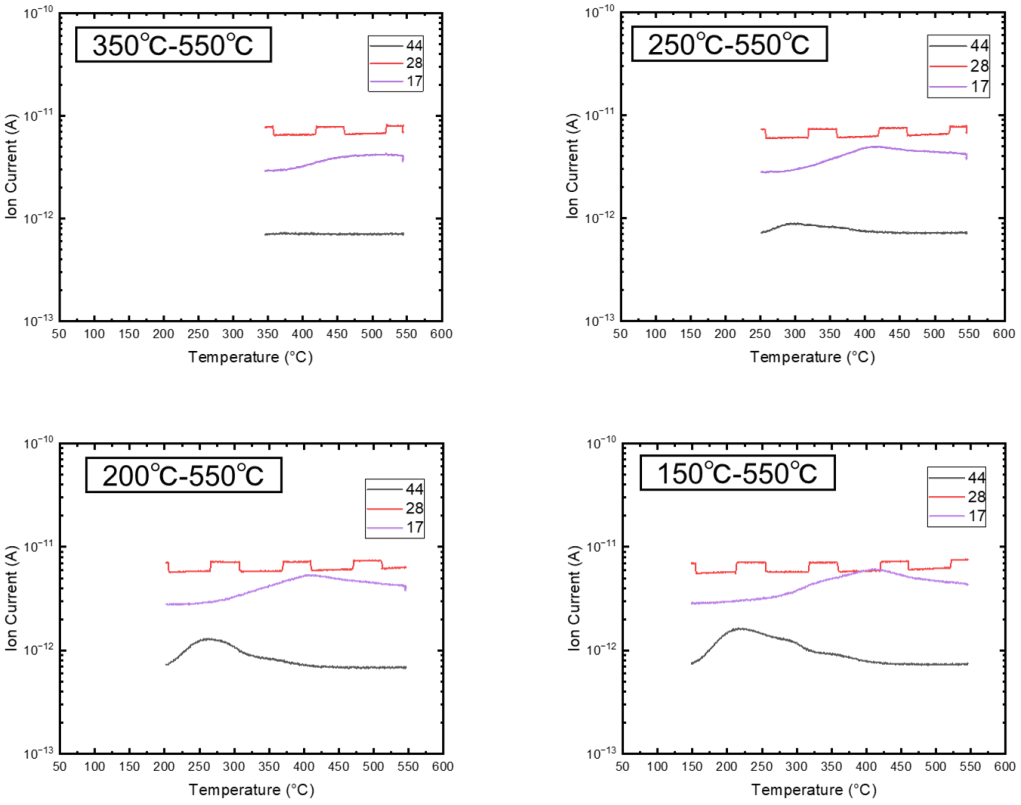

Fig. 4.19 CO-TPR measurement of fine SnO_2.

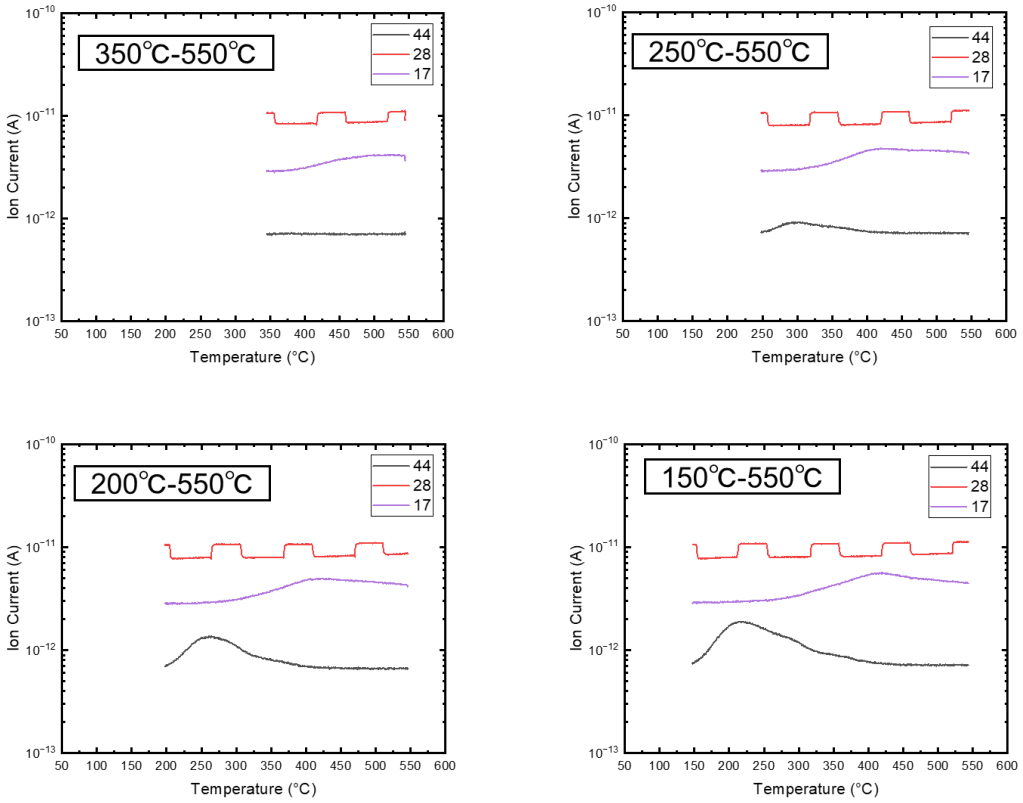

Fig. 4.20 CO-TPR measurement of coarse SnO_2.

(2) Pd-loaded SnO_2

Fig. 4.21 and 4.22 show the GC-MS of Pd-loaded fine and coarse SnO_2. Temperatures above 100ºC do not cause deterioration by CO. The temperatures below 100ºC occur the deterioration as occurred in the non-loaded sample. Fig. 4.23 illustrates the catalytical combustion of non-loaded SnO_2 and Pd-loaded SnO_2. The Pd-loaded SnO_2 behavior was equal for fine and coarse Pd-SnO_2, same tendency encountered in gas-sensing. Therefore, electronic, and chemical sensitization occur on both fine and coarse SnO_2 in the same manner.

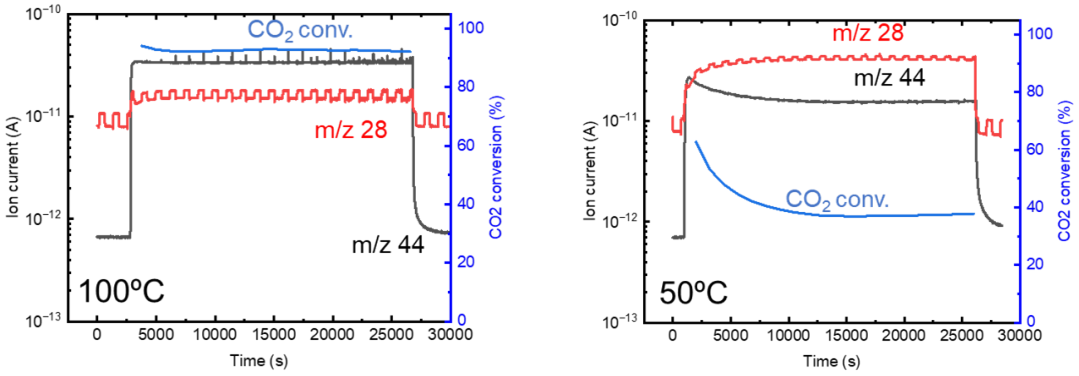

Fig. 4.21 Catalytical combustion of Pd-loaded fine SnO_2 in CO gas flow.

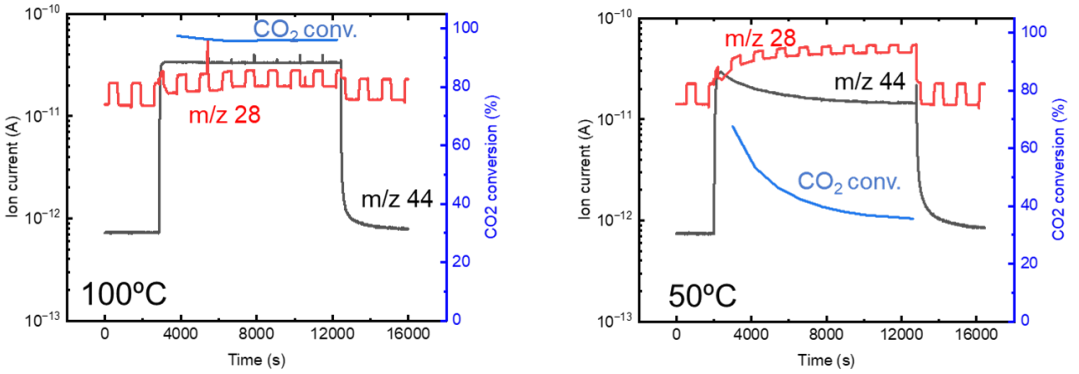

Fig. 4.22 Catalytical combustion of Pd-loaded coarse SnO_2 in CO gas flow.

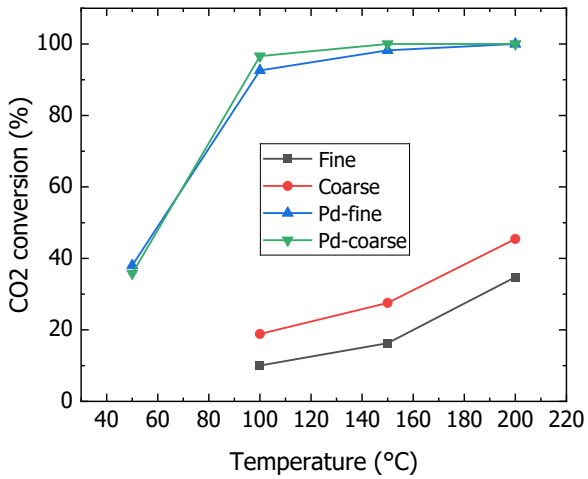

Fig. 4.23 Temperature dependence of Pd-loaded fine and coarse in CO catalytical combustion.

Regarding TPR results, the Pd-loaded fine and coarse SnO_2 both have similar TPR behavior, as shown in Fig. 4.24 and 4.25. The gas introduction operated at a temperature above 100ºC does not show a considerable peak, which has the same behavior as CO-TPR 350-550ºC of the non-loaded sample. At CO-TPR 100-550ºC moderate peak appears at 150ºC and a sharp peak appears at 100ºC when operating TPR with 50-550ºC. This first accentuated peak is equivalent to CO or CO_2 physisorption peak, as visualized also in neat-SnO_2. Even though was mild, the three peaks were still in both curves. Therefore, Pd mitigates the CO reduction property on SnO_2, avoiding the specific and undetermined chemisorption on SnO_2 (two broad peaks in 275ºC and 350ºC).

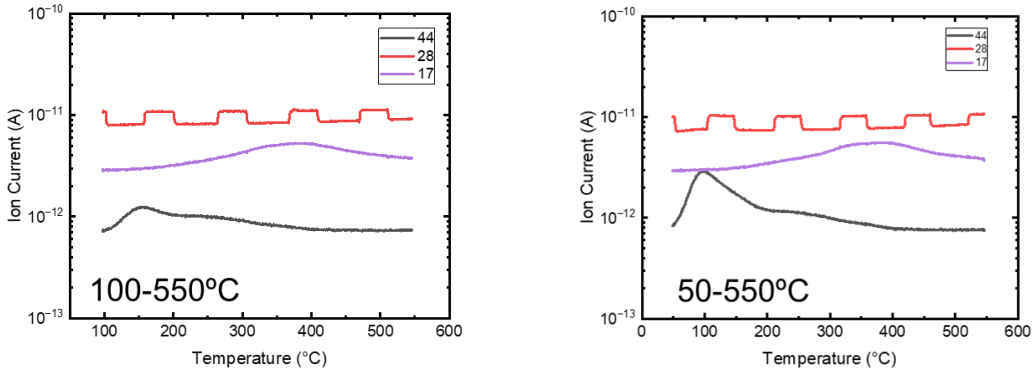

Fig. 4.24 CO-TPR measurement of Pd-loaded fine SnO_2 in.

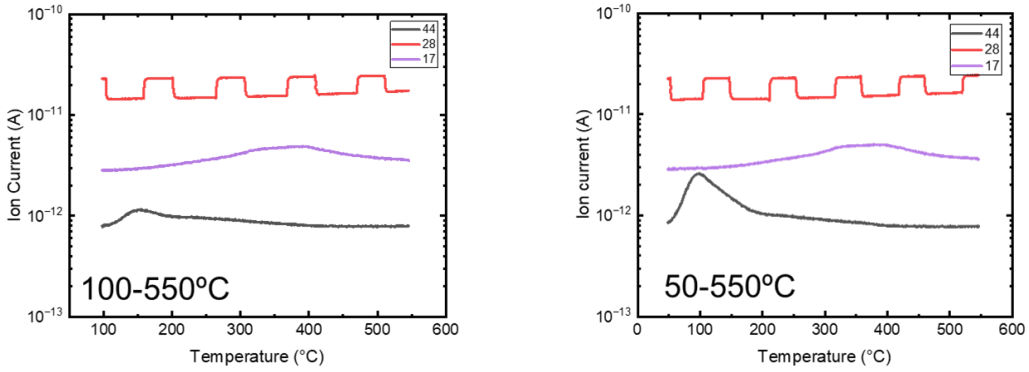

Fig. 4.25 CO-TPR measurement of Pd-loaded coarse SnO_2.

4.6 Summary

In this chapter, the electrical and gas-sensing properties were evaluated for separated SnO_2, in thick film sensor and MEMS gas sensor. Moreover, the catalytical combustion and TPR measurement to clarify the chemical reaction differences in the secondary particle size variation.

The following summarized the knowledge acquired:

(1) The inter-primary particle and bulk resistance are important resistive components in gas sensors that are sensitive to surface charge modification.

(2) The fine and coarse SnO_2 are plausible for MEMS gas sensors, presenting high reproducibility. Nevertheless, the fine SnO_2 is better to adjust the thickness for VOC gas detection or simply use a middle-size SnO_2.

(3) The high electrical resistance in coarse SnO_2 is explained by electron conduction path number and percolation threshold theory.

(4) The high sensor response in fine SnO_2 is explained by effective Knudsen diffusion. In this case, the inter-secondary particle of coarse SnO_2 can be sensitive to surface charge modification, or the inter-primary particle resistance is fragmented in sensitive and non-sensitive resistive components, in terms of the model of resistive components in gas sensors.

(5) The CO gas has a peculiar reduction property against the SnO_2 surface. In neat-SnO_2, the deterioration starts from 300ºC. However, in Pd-SnO_2, this is lessened to 100ºC. Therefore, Pd avoids the CO reduction property on the SnO_2 surface.

5. Conclusions

5.1 Conclusion

Metal oxide semiconductor gas sensor is a widely studied device to detect low gas concentration with high thermal and chemical stability. Our laboratory and others related to research on this device established several key factors in designing high-performance gas sensors. This includes the transducer function, receptor function, and utility factor. With the technology transition to IoT, a new requirement appears on this device, mainly the miniaturization for low consumption and packaging. The current material is not appropriate for miniaturization, because it does not care about the micro-size effect. Even having or not some micro-size effect responsible for gas-sensing, the non-controlled micro-size mitigates the key factor design, mainly the utility factor. This research investigated the secondary particle size effect on electrical resistance and gas-sensing, aiming to determine a material apt to miniaturization.

In Chapter 1, we explained the metal oxide semiconductor gas sensor focused on SnO2 and the three principal key factors to design a high-performance gas sensor. In addition, the miniaturized gas sensor device presentation and the sophisticated use by pulse-driven temperature modulation.

In Chapter 2, we detailed the material synthesis methods of SnO_2, and the classification method operated on it. Additionally, the characterization method of synthesized material was detailed and the gas sensor system and configuration as well.

In Chapter 3, it was applied a screening of SnO_2 for classification, with uniform particle size distribution on non-separated SnO_2 and narrow particle size distribution on separated SnO_2. The hydrothermal synthesis method creates many extremely large particles that difficult the analysis of fine particles. In contrast, the ethanol rinse method creates many extraordinarily fine particles that difficult the analyze coarse particles. The selected SnO_2 for classification was synthesized by non-hydrothermal synthesis and no ethanol substitution. These show uniform particle size distribution with relatively narrow particle size distribution, however still broader for fine, according to the laser scattering method. Even though not selected, the extremely coarse particle size is appropriate for catalytical combustion with high resolution and the extremely fine particle size might be appropriate to a miniaturized gas sensor.

In Chapter 4, it was measured and analyzed the electrical resistance and gas-

sensing of fine and coarse SnO_2. The fine SnO_2 gas sensor obtained low electrical resistance and higher sensor response than coarse SnO_2, more appropriate for the miniaturized gas sensor. However, in large molecular gases such as VOC gas, the thickness of fine SnO_2 becomes an important factor because it is difficult to diffuse into the region near the electrode of the sensitive membrane with a relatively thick film. Therefore, the ideal sensitive membrane for miniaturized gas sensors is:

(1) The particles near the electrode are constituted by fine secondary particles, around 50% or less of the electrode distance.

(2) The particle size will gradually be larger in the region distant from the electrode.

For (1), the inter-secondary particle resistance and the inter-primary particle resistance components require to be separately analyzed, using the EIS varying the electrode distance, ideally at micron size. For (2), the chemical difference between fine and coarse needs to be clarified, at least the surface charge difference.

As described above, the size of the secondary particles plays a crucial role in the manufacturing of gas sensors, particularly for miniaturized ones. This factor also contributes to improved accessibility at low temperatures and enhances reproducibility.

Reference

(1) Overview of the High Pressure Gas Safety Act, *The High Pressure Gas Safety Institute of Japan (KHK)*
https://www.khk.or.jp/Portals/0/resources/english/dl/overview_hpg_act.pdf

(2) Annual Report on Liquefied Petroleum Gas (LPG) Related Accidents, *The High Pressure Gas Safety Institute of Japan (KHK)*
https://www.khk.or.jp/english/report.html

(3) Understanding VOC Gas and Its Impact on the Environment, *Environics*,
https://www.environics.com/2023/04/10/understanding-voc-gas-impact-on-environment/

(4) W. H. Brattain, W. H. Bardeen, *Bell Syst. Tech. J.* **32**, 1-41 (1952).

(5) S. R. Morrison, *J. Phys. Chem*, **57**, 860 (1953).

(6) T. Seiyama, A. Kato, K. Fujiishi, M. Nagatani, *Anal. Cham.*, **34**, 1502 (1962).

(7) 田口尚義、特公昭 45-38200(出願昭 37).

(8) VOC 排出削減効果の検討等業務報告書、一般社団法人産業環境管理協会.

(9) K. Suematsu, W. Harano, T. Oyama, Y. Shin, K. Watanabe, K. Shimanoe, *Anal. Chem.*, **90**, 19, 11219-11223 (2018).

(10) M. V. Nikolic, V. Milovanovic, Z. Z. Vasiljevic, Z. Stamenkovic, *Sensors*, **20**, 6694 (2020).

(11) B. Buszewski, M. Kesy, T. Ligor, A. Amann, *Biomed. Chromatogr.*, 21, 553-566 (2007).

(12) G. Konvalina, H. Haick, *Acc. Chem. Res.*, **47**, 1, 66-76 (2014).

(13) R.A. Potyrailo, *Chem. Rev.*, 116, 11877-11923 (2016).

(14) A. Dey, *Mater. Sci. Eng. B*., **229**, 206-217 (2018).

(15) 清山哲郎、化学センサ実用便覧、フジ・テクノシステム (1986).

(16) D.N Oosthuizen, D.E. Motaung, H.C. Swart, *Appl. Surf. Sci.*, **505**, 144356 (2020).

(17) T. Itoh, Y. Taguchi, N. Izu, I. Matsubara, S. Nakamura, K. Suzuki, K. Kanda, W. Shin, M. Nishibori, *Sens. Lett.*, **9** (2), 703-705 (2011).

(18) K. Tanaka, A. Ozaki, *J. Catalysis*, 8, 2 (1967).

(19) M. Iwamoto, Y. Yoda, N. Yamazoe, T. Seiyama, *J. Phys. Chem.*, **82** (24), 2564-2570 (1978).

(20) M. Egashira, S. Deguchi, S. Kagawa, *Reports of the Faculty of Engineering, Nagasaki University*, **6**, 129 (1975).

(21) 大隈信行, 舟山義一, 伊藤宏, 水谷惟恭, 加藤誠軌, 表面化学, **9**, 452 (1988).

(22) A. Staerz, U. Weimar, N. Barsan, *Sens. Actuators B Chem.*, **358**, 131531 (2022).

(23) Z. Hua, M. Yuasa, T. Kida, N. Yamazoe, K. Shimanoe, *Chem. Lett.*, **43**, 1435-1437 (2014).

(24) T. Yamanaka, R. Kurashima, J. Mimaki, *Z. Kristallogr.*, **215**, 424-428 (2000).
(25) M. Batzill, U. Diebold, *Prog. Surf. Sci.*, **79**, 47-154 (2005).
(26) C. Kallic, A. Zunger, *Phys. Rev. Lett.*, **88**, 095501 (2002).
(27) T. Sahm, A. Gurlo, N. Barsan, U. Weimar, *Sens. Actuators B: Chem.*, **118**, (1-2), 78-83 (2006).
(28) N. Barsan, D. Koziej, U. Weimar, *Sens. Actuators B: Chem.*, **121**, 18-35 (2007).
(29) N. Ma, K. Suematsu, M. Yuasa, T. Kida, K. Shimanoe, *ACS Appl. Mater. Interfaces*, **7**, 5863-5869 (2015)
(30) N. Yamazoe, K. Suematsu, K. Shimanoe, *Sens. Actuators B: Chem.*, **163**, 128-135 (2012).
(31) N. Yamazoe, K. Suematsu, K. Shimanoe, *Sens. Actuators B: Chem.*, **176**, 443-452 (2013).
(32) N. Yamazoe, J. Fuchigami, M. Kishikawa, T. Seiyama, *Surf. Sci.*, **86**, 335-344 (1979).
(33) J. Tamaki, M. Nagaishi, Y. Teraoka, N. Miura, N. Yamazoe, K. Moriyama, Y. Nakamura, *Surf. Sci.*, **221**, 183-196 (1989).
(34) N. Yamazoe, K. Shimanoe, *J. Sensors*, article ID 875704, 1-21 (2009).
(35) Y. Mizokawa, S. Nakamura, *Jpn. J. Appl. Phys*., **14**, 779 (1975).
(36) S. Lenaerts, J. Roggen, G. Maes, *Spectrochim. Acta. Mol. Biomol. Spectros*., **51**, 883 (1995).
(37) B. Gillot, C. Fey, D. Delafosse, *J. Chem. Phys.*, **73**, 19 (1976).
(38) K. Suematsu, M. Yuasa, T. Kida, N. Yamazoe, K. Shimanoe, *J. Electrochem. Soc.*, **161**, B123 (2014).
(39) E. W. Thornton, P. G. Harrison, *J. Chem. Soc., Faraday Trans. 1*, **71**, 461-472 (1975).
(40) D. Kohl, *Sens. Actuators*, **18**, 71-113 (1989).
(41) 末松 昂一、博士論文（九州大学） (2012).
(42) T. Krishnakumar, R. Jayaprakash, N. Pinna, A. Donato, N. Donato, G. Micali, G. Neri, *J. Sensors*, **2009**, Article ID 980965 (2009).
(43) Nan Ma, Doctoral dissertation (Kyushu University)（2015）.
(44) N. Yamazoe, G. Sakai, K. Shimanoe, *Catal. Surv. Asia*, **7**, 63-75 (2003).
(45) 山添舜, 電子技術, **25**, 44 (1983).
(46) N.Yamazoe, Y. Kurokawa, T. Seiyama, *Sens. Actuators*, **4**, 283-289 (1983).
(47) CN. Xu, J. Tamaki, N. Miura, N. Tamazoe, *J. Electrochem. Soc.*, **143**, 148-150 (1996).
(48) S. Matsushima, Y. Teraoka, N. Miura, N. Yamazoe, *Jpn. J. Appl. Phys*., **27**, 1798-1802 (1988).
(49) N. Yamazoe, *Sens. Actuator B: Chem.*, *5*, 7-19 (1991).
(50) N.Yamazoe, *Shokubai*, **28**, 555-559 (1986).
(51) C. Xu, J. Tamaki, N. Miura, N. Yamazoe, *Sens. Actuators B: Chem.*, **3**(2), 147-155 (1991).
(52) C.N. Xu, J. Tamaki, N. Miura, N. Yamazoe, *Chem. Lett.*, **3**, 441 (1990).
(53) N. Yamazoe, K. Shimanoe, *Sens. Actuators B: Chem.,* **128**, 566 (2008).

(54) N. Yamazoe, K. Shimanoe, *J. Elec. Soc.*, **155**, J85 (2008).
(55) P. K. Clifford, D.T. Tuma, *Sens. Actuator*, **3**, 233-254 (1982).
(56) N. Matsunaga, G. Sakai, K. Shimanoe, N. Yamazoe, *Sens. Actuators B: Chem.*, **83**, 216-221 (2002).
(57) G. Sakai, N. Matsunaga, K. Shimanoe, N. Yamazoe, *Sens. Actuators B: Chem.*, **80**, 125-131 (2001).
(58) N. Matsunaga, G. Sakai, K. Shimanoe, N. Yamazoe, *Sens. Actuators B: Chem.*, **96**, 226-233 (2003).
(59) N. Yamazoe, G. Sakai, K. Shimanoe, *Cat. Surv. Asia*, **7**, 63 (2003).
(60) T. Kida, K. Suematsu, K. Hara, K. Kanie, and A. Muramatsu, *ACS Appl. Mater. Interfaces,* **8**, 51 (2016).
(61) T. Kida, S. Fujiyama, K. Suematsu, M. Yuasa, K. Shimanoe, *J. Phys. Chem. C*, **117** (34), 17574-17582 (2013).
(62) S. Feng, F. Farha, Q. Li, Y. Wan, Y. Xu, T. Zhang, H. Ning, *Sensors*, **19**(17), 3760 (2019).
(63) S. Huang, A. Croy, L. A. Panes-Ruiz, V. Khavrus, V. Bezugly, B. Ibarlucea, G. Cuniberti, *Adv. Intell. Syst.*, **4**, 2200016 (2022).
(64) K. Izawa, *Electrochemistry*, **84**, 282 (2015).
(65) K. Yoshioka, T. Tanihira, K. Shinnishi, K. Kaneyasu, *Chem. Sensors*, **23**, 16 (2007).
(66) J. Li, Y. Peng, Y. Li, W. Li, Y. Jin, Z. Tang, Y. Duan, Clin. Chim. Acta., 436, 59-67 (2014).
(67) S. M. Gordon, J. P. Szidon, B. K. Krotoszynski, R. D. Gibbons, H. J. O'Neill, *Clin. Chem.*, **31**, 1278 (1985).
(68) M. Todaka, K. Hirabayashi, A. Kawanishi, M. Morimachi, Y. Sekine, *Jpn. J. Clin. Ecol.*, **30**(1), 7-16 (2021)
(69) M. Kinoyama, H. Nitta, A. Watanabe, H. Ueda, *J. Heal. Sci.*, **54**(4), 471-477 (2008).
(70) H. L. Vine, US Patent 3906473 (1975).
(71) Y. Sun. X. Huang, F. Meng, J. Liu, *Sensors*, **4**, 95 (2004).
(72) M. Schweizer-Berberich, M. Zdralek, U. Weimar, W. Gopel, T. Viard, D. Martinez, A. Seube, A. Peyre-Lavigne, *Sens. Actuators B: Chem.*, **65**, 1 (2000).
(73) K. Suematsu, W. Harano, T. Oyama, Y. Shin, K. Watanabe, K. Shimanoe, *Anal. Chem.*, **90**, 11219 (2018).
(74) K. Suematsu, W. Harano, S. Yamasaki, K. Watanabe, K. Shimanoe, *ACS Appl. Elec. Mater.*, **2**(12), 4122-4126 (2020)
(75) T. Sasahara, M. Nishimura, H. Ishihara, K. Toyoda, T. Sunayama, S. Uematsu, T. Ozawa, K. Ogino, M. Egashira, *Electrochem.*, **71**, 457 (2003).
(76) T. Hyodo, T. Hiura, K. Nagae, K. Kamata, T. Ueda, Y. Shimizu, *Chem. Sens.*, **35** (2018).
(77) T. Hyodo, S. Abe, Y. Shimizu, M. Egashira, *Sens. Actuators B: Chem.*, **93**, 590-600 (2003).
(78) J. Tamaki, A. Miyaji, J. Makinodan, S. Ogura, S. Konishi, *Sens. Actuators B: Chem.*,

108, 202-206 (2005).
(79) 江藤守總, 機器分析の基礎, 裳華房 (1998).
(80) Carbon dioxide mass spectrum, NIST Chemistry WebBook, SRD 69 (NIST Mass Spectrometry Data Center, U.S. Secretary of Commerce).
(81) Water mass spectrum, NIST Chemistry WebBook, SRD 69 (NIST Mass Spectrometry Data Center, U.S. Secretary of Commerce).
(82) N. Yamazoe, K. Shimanoe, *Sens. Actuators B: Chem.*, **160**, 1352-1362 (2011).
(83) T. Kida, T. Doi, K. Shimanoe, *Chem. Matter.*, **22**, 2662-2667 (2010).
(84) A. Vertanessian, A. Allen, M. J. Mayo, *J. Mater. Res.*, **18(2)**, 495-506 (2003).
(85) N. Yamazoe, *Sens. Actuators B: Chem.*, **108**, 2-14 (2005).
(86) E. Trenkenschuh, W. Friess, *Eur. J. Pharm. Biopharm.,* **165**, 345-360 (2021).
(87) E. Ghobadi, A. Marquardt, E.M. Zirdehi, K. Neuking, F. Varnik, G. Eggeler, H. Steeb, Inter. J. Polym. Sci., ID 7819353 (2018)

Acknowledgments

I extend my deep gratitude to all who selflessly supported me in writing this thesis.

My deepest gratitude first and foremost goes to Professor Kengo Shimanoe, my supervisor, for his constant attention and guidance. Without his consistent and illuminating instruction, this thesis could not have reached its present form.

Secondly, I want to express my sincere gratitude to all my teachers who provided me with valuable academic and life guidance, especially Professor Koichi Suematsu, Professor Ken Watanabe, and Mrs. Yoshida.

My sincere thanks also go to all the former and present members of the laboratory: Mrs. Hoshino, Mrs. Shinagawa, Ms. Yang, Mr. Ren, Mr. Yanagawa, Mr. Kamitani and Mr. Takeno, especially for encouraging words and time in teaching me, and helping me work out my problems. I also feel grateful to all the other fellows: Mr. Kobayashi, Mr. Kunisaki, Mr. Naito, Mr. Fukuno and Mr. Nakashima.

My sincere thanks also go to Monbukagakusho (MEXT) for financial support via the MEXT research/graduate student scholarship.

Finally, my thanks go to my family for their psychological support and encouragement during my master's course in Japan.